REPORT DOCUMENTATION PAGE

Form Approved OMB No. 0704-0188

Public reporting burden for this collection of information is estimated to average 1 hour per response, including the time for reviewing instructions, searching existing data sources, gathering and maintaining the data needed, and completing and reviewing the collection of information. Send comments regarding this burden estimate or any other aspect of this collection of information, including suggestions for reducing the burden, to Department of Defense, Washington Headquarters Services, Directorate for Information Operations and Reports (0704-0188), 1215 Jefferson Davis Highway, Suite 1204, Arlington, VA 22202-4302. Respondents should be aware that notwithstanding any other provision of law, no person shall be subject to any penalty for failing to comply with a collection of information if it does not display a currently valid OMB control number.
PLEASE DO NOT RETURN YOUR FORM TO THE ABOVE ADDRESS.

1. REPORT DATE *(DD-MM-YYYY)* 08-10-2004	2. REPORT TYPE Final Report	3. DATES COVERED *(From – To)* 9 March 2001 - 09-Mar-04

4. TITLE AND SUBTITLE Novel, Solvent Free, Single Ion Conductive Polymer Electrolytes	5a. CONTRACT NUMBER F61775-01-WE020
	5b. GRANT NUMBER
	5c. PROGRAM ELEMENT NUMBER
6. AUTHOR(S) Professor Emanual Peled	5d. PROJECT NUMBER
	5d. TASK NUMBER
	5e. WORK UNIT NUMBER

7. PERFORMING ORGANIZATION NAME(S) AND ADDRESS(ES) Tel Aviv University Ramat Aviv, Tel Aviv 699978 Israel	8. PERFORMING ORGANIZATION REPORT NUMBER N/A
9. SPONSORING/MONITORING AGENCY NAME(S) AND ADDRESS(ES) EOARD PSC 802 BOX 14 FPO 09499-0014	10. SPONSOR/MONITOR'S ACRONYM(S)
	11. SPONSOR/MONITOR'S REPORT NUMBER(S) SPC 01-4020

12. DISTRIBUTION/AVAILABILITY STATEMENT

Approved for public release; distribution is unlimited.

13. SUPPLEMENTARY NOTES

14. ABSTRACT

This report results from a contract tasking Tel Aviv University as follows: The main task of this project is to design and characterize novel types of lithium conducting polymer electrolytes. This task will be pursued by the combined efforts of three academic groups having world-wide recognized experience in polymer electrolyte science, namely, the Group of Professors Wladyslaw Wieczorek and Florjanczyk of the Warsaw University of Technology in Poland, the Group of Professor Emanuel Peled at the University of Tel Aviv, Israel and the Group of Professor Bruno Scrosati at the University 'La Sapienza' of Rome, Italy. Broadly, the Polish Group will be involved in the synthesis of the new polymer electrolytes; the Italian Group will act as the coordinator of the Project, in their basic electrochemical characterization; and the Group in Israel in the fabrication and test of laboratory cell prototypes.

The work plan that will be specifically carried out at the School of Chemistry, Tel Aviv University will involve the following items: 1) Characterization of polymer in salt electrolytes provided by the Warsaw Group with the use of MDSC, TOF SIMS, XRD, SEM and XPS; 2) Developing procedures for the preparation of composite cathodes and coin type lithium cells with high conductive polymer electrolytes; and 3) Characterization of the coin cells. Two cathode materials will be used for electrolyte evaluations: 1) Pyrite; 2) LiCoO2.

15. SUBJECT TERMS
EOARD, Power, Electrochemistry, Batteries

16. SECURITY CLASSIFICATION OF:			17. LIMITATION OF ABSTRACT UL	18, NUMBER OF PAGES	19a. NAME OF RESPONSIBLE PERSON WAYNE A. DONALDSON
a. REPORT UNCLAS	b. ABSTRACT UNCLAS	c. THIS PAGE UNCLAS		57	19b. TELEPHONE NUMBER *(Include area code)* +44 (0)20 7514 4299

Standard Form 298 (Rev. 8/98)
Prescribed by ANSI Std. Z39-18

FINAL REPORT

Contract No F61775-01-WE020

SPC 01-4020 "NOVEL, SOLVENT FREE, SINGLE ION CONDUCTIVE POLYMER ELECTROLYTES"

For the period from 01. 02. 2001 to 18. 08. 2004

Principal investigators: Prof. E. Peled

Prof. D. Golodnitsky

School of Chemistry, Tel Aviv University,

Tel Aviv, 69978, Israel

August 2004

ABSTRACT

PART 1. Development and characterization of thin-film iron sulfide cathodes for lithium and lithium-ion batteries

Characterization of four types of FeS_2-cathodes for the Li/CPE/pyrite battery was carried out by SEM, X-ray photoelectron spectroscopy (XPS), X-ray diffraction (XRD), and electrochemical methods.

Analysis of the experimental data, suggests that for pyrite-based cathodes (obtained by casting, doctor-blade technique and RF sputtering) it is the mass transport of iron cations through the Li_2FeS_2 that slows the charge rate and creates a charge overvoltage. Formation of sulfur vacancy-rich pyrite structure eliminates transport limitations of iron in Li_2FeS_2 and shows promise for the design of cathodes for high-energy-density lithium batteries. Formation of cathode SEI prevents undesirable reactions from occurring at deep discharge and increases the long-term stability of the Li/FeS_2 cells.

The electrochemically deposited cathode is a mixture of iron mono- and disulfide, and non-stoichiometric FeS_{1+x} phases with some iron oxides. XRD and XPS tests showed that 0.6-1μm thick FeS_{1+x} films were amorphous, with network-like porous structure, comprising nano-size particles. The Fe:S stoichiometry of the films was invariant with depth. $Li/CPE/FeS_{1+x}$ cells ran at $i_d = i_{ch} = 50$ $\mu A/cm^2$ (c/1 rate) and 125°C for over 650 charge/discharge cycles with 0.06% per cycle capacity loss and 100% Faradaic efficiency. On the basis of the experimental data it can be deduced that this simple electrodeposition method shows great promise for the preparation of ultra-thin cathodes for microbattery applications.

PART 2. Development and characterization of single-lithium conducting polymer electrolytes.

The second part of our research work was focused on increasing the t_+ of PEO-based polymer electrolytes by anion immobilization with calixarene, which was produced by the Warsaw research group. Three types of calixarene additive ($C_{72}H_{96}N_4O_6$ calixarene A, $C_{72}H_{94}N_6O_{10}$ –calixarene B, and $C_{68}H_{104}N_4O_6$ -calixarene C) were tested. It was found that the structure and morphology of LiI $P(EO)_n$ polymer electrolytes depend strongly on the type of calixarene and its concentration. The total ionic resistance of the Li/PE/Li cell with a high concentration of calixarene A is greater than that of the other samples. The transference number measured at about 50°C for the additive-free PE was 0.35 to 0.5,

depending on the test conditions. For the electrolyte containing calixarene A, the maximal lithium-ion transference number (0.6) was detected for the PE with 1:0.3 LiI:calixarene A ratio. Unit value of t_+ was achieved for a PE with a 1:1 LiI:calixarene B ratio. We believe that this results from the immobilization of the iodide ion by calixarene and the possible ordering of the polymer-salt complex.

Introduction

The work plan carried out at the School of Chemistry, Tel Aviv University involves the following:

1. Working out procedures for the preparation of thin-film pyrite cathodes and constructing coin-type lithium cells with highly conductive polymer electrolytes. Characterization of cathodes with the use of MDSC, XRD, SEM and XPS methods.
2. Electrochemical characterization of the coin cells.
3. Characterization of polymer-in-salt electrolytes and studying the effect of calixarene additives provided by the Warsaw Group, on the structure, thermal stability and electrochemical properties of solid polymer electrolytes.

PART 1. DEVELOPMENT AND CHARACTERIZATION OF THIN-FILM IRON SULFIDE CATHODES FOR LITHIUM AND LITHIUM-ION BATTERIES

Thin-film (mainly lithium-based) battery research began in earnest about two decades ago, with the most significant work done since about 1992 in the USA at the Oak Ridge National Laboratory by a group led by J. D. Bates [1]. Thin films result in higher current densities and cell efficiencies, because the transport of ions is easier and faster through thin-film layers than through thick layers. At present, the main techniques for making thin-film cathodes include chemical vapor deposition (CVD), sputtering, spray pyrolysis and evaporation. Some of these processes are typically carried out at high temperatures. There is a need to provide an inexpensive and relatively simple method, operable at near-ambient temperatures, for preparing thin cathode layers that are pure phases free of binders.

This study is focused on the development of a procedure for the preparation of thin-film iron sulfide cathodes by RF sputtering and electrodeposition. The charge-discharge mechanism in the all-solid-state lithium/composite polymer electrolyte/pyrite battery operating at 120°C is investigated.

In order to clarify the redox and insertion kinetics of pyrite and to estimate the compatibility of FeS_2 reduction products and CPE, four types of cathodes were tested: composite CPE-bonded cathodes prepared by casting and doctor-blade methods, Teflon-bonded cathodes and 100% dense (composed of the active material alone) pure pyrite obtained by RF sputtering and electrodeposition methods.

CAST AND RF-SPUTTERED CATHODES

Iron sulfide (FeS_2) has been investigated as a positive-electrode material in thermal, nonaqueous and polymer-electrolyte lithium batteries and several charge-discharge mechanisms have been discussed. In nonaqueous and molten media as well as in polymer electrolytes, the discharge of FeS_2 was thought to proceed as a multi-stage process with the formation of metallic iron and lithium sulfide as the final discharge products. The $Li_3Fe_2S_4$, $Li_{11}Fe_4S_{10}$ and Li_2FeS_2 intermediates were detected on reversible charge-discharge of high-temperature (450°C) pyrite cells with LiCl/KCl eutectic molten electrolytes [2]. For the Li/pyrite system in nonaqueous electrolyte, the formation of Li_3FeS_4 [3], Li_2FeS_2 [4, 5] or FeS [6] during discharge was suggested. It has been shown [7-9] that Li_2FeS_2 can be de-intercalated during charge with the formation of $Fe^{3+}(S_2^{2-})_{1/2} S^{2-}$ final structure. All the room-temperature cells showed extremely poor reversibility or none at all [3-6, 10].

Good reversibility of Li/composite polymer electrolyte (CPE)/FeS_2 cells was obtained over the temperature range of 90 to 135 °C [11]. From the analysis of dq/dV curves [12] and EXAFS and NEXAFS tests [13], it was deduced that the reduction of ferrous disulfide proceeds as a multi-stage process, via Li_2FeS_2, to metallic iron. No evidence of FeS was found. Two distinctive features characterize the reversible reduction of pyrite in composite polymer electrolyte. The first is a sudden voltage jump at about 1.85V that occurs on charging. The second is the appearance of a low-voltage 1.3V plateau and the progressive increase of its contribution to the overall charge/discharge process. This is followed by a decrease in the specific energy of the battery. Several attempts were made to explain these phenomena [12-14], however, there is much still to be learned.

In this work, elucidation of the charge-discharge mechanism in the Li/(CPE)/FeS_2 battery has continued.

Experimental

The electrochemical cells studied comprise a lithium anode, $LiI_1P(EO)_{20}EC_1$, 12% by volume (v/v) Al_2O_3 composite polymer electrolyte and a 35 to 100% v/v pyrite-based cathode. The electrolytes were prepared from poly(ethylene oxide) (P(EO)) (Aldrich, average molecular weight $5x10^6$), which had been vacuum dried at 45 to 50 °C for about 24 hours. The LiI (Aldrich) was vacuum dried at 150 °C for about 8 hours. All subsequent handling of these materials took place under an argon atmosphere in a VAC glove box containing less than 10 ppm water. The detailed procedure of the polymer electrolyte preparation has been described elsewhere [11-13].

In our previous studies the 10-15 μm-thick cathode foil was prepared by dispersing fine natural pyrite powder (Chemalloy less than 10 μm size particles) in a polymer electrolyte slurry and cast on a teflon tray. Grinding of pre-dried pyrite was performed in a hermetically sealed ball mill for 48 hours. On casting of the composite cathode, FeS_2 tends to settle to the bottom, as its density is twice as that of the PE. The distribution of pyrite over the thickness of the cast cathode is, therefore, non-homogeneous (Fig.1a).

a
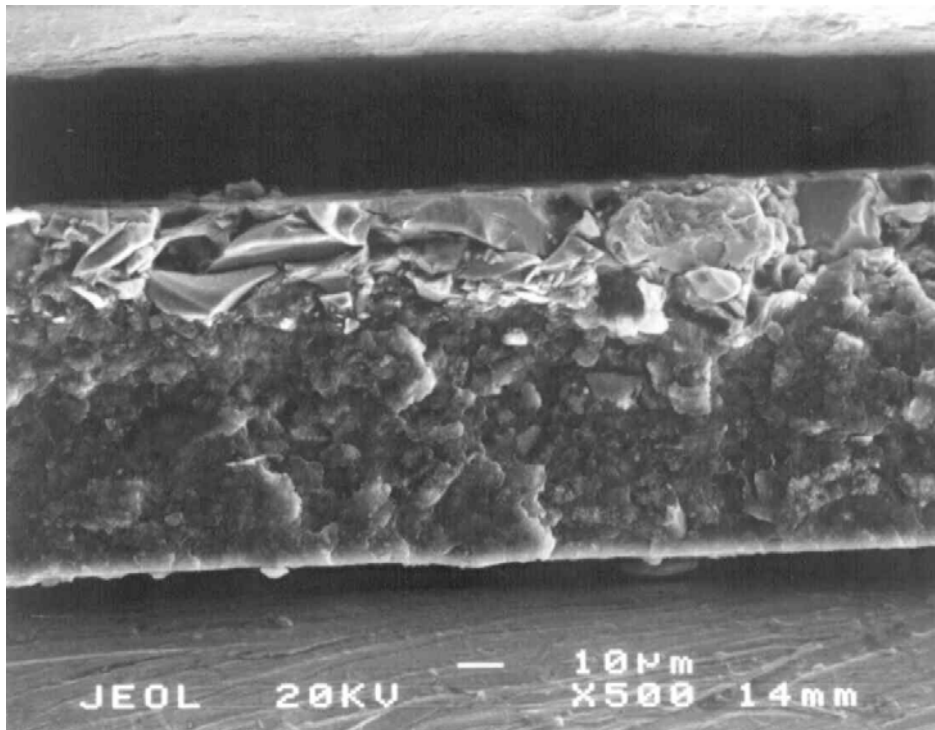
FeS$_2$

CPE-phase

b
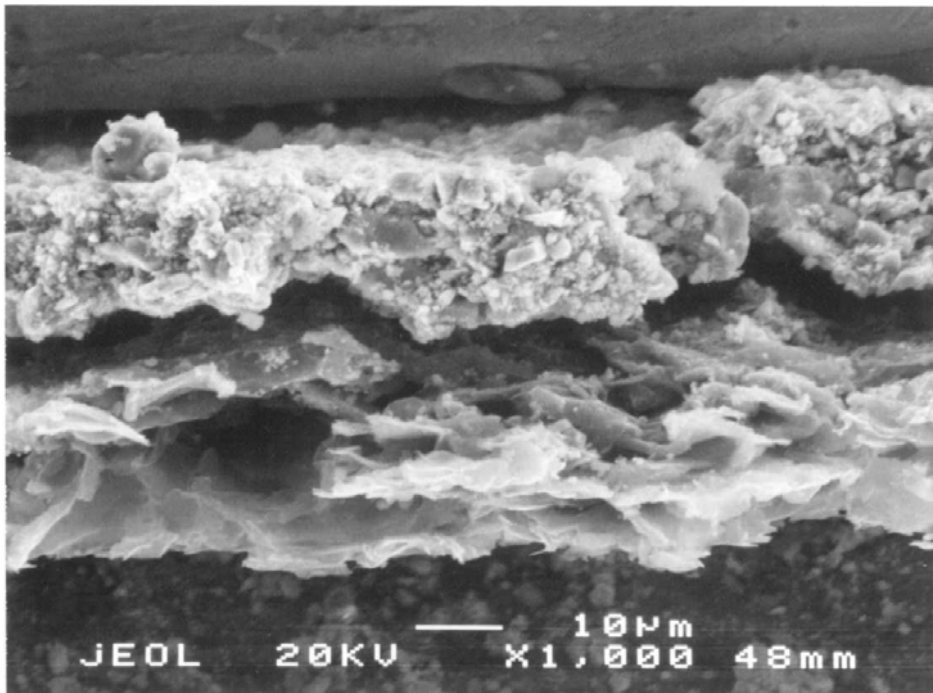
Cathode

Graph-foil   current
collector

Fig. 1. SEM images of cross-section of as-cast composite cathode before
hot pressing (a) and DB-cathode on graph foil (b)

We addressed the problem in two ways. In the first stage of our work an effort was made to adapt the doctor-blade (DB) technique, which is a commonly used method for the preparation of homogeneous battery cathodes, to the fabrication of thin-film pyrite-based composite cathodes. Composite cathodes were prepared by the addition of 35 to 80% (v/v) pyrite to a CPE or a mixture of 10% (v/v) teflon and 5% (v/v) SiO_2 in cyclopentanone. The blended paste was poured on the graph foil and spread uniformly with the doctor blade (DB). Composite cathodes were dried in vacuum at 70 ºC for 8 hours. As can be seen from the SEM micrographs (Fig. 1b) the pyrite is homogeneously distributed in the CPE network of the DB cathode. The exfoliation of the graph foil, seen in the lower part of this image, is caused by quenching in liquid nitrogen, which was used for cross-section cutting of the cathode.

The second approach was directed towards the development of a procedure of RF sputtering (RFS) of ultra-thin 100% dense cathodes. Cycling of such cathodes allows rapid characterization of the performance of battery components. Such cathodes can be used in microbatteries as well. Ultra-thin (about 1μm-thick) cathodes were prepared by RF sputtering (RFS) a pyrite target with the use of a Pfeiffer Vacuum PLS 160 instrument. RF power was 25W, pressure $5*10^{-7}$ torr, time of sputtering 6 hours. The thickness of the 100% dense cathode, as measured by a profilometer was about 9000 ±50Å.

Carefully following all the steps of cathode preparation, we succeeded in obtaining reproducibility of battery performance (utilization of cathode-active material, reversible capacity, charge-discharge overpotential) in the range of 2-5 %.

The 0.95 cm^2 cells composed of a lithium anode, a 100-150 μm CPE film and a composite cathode were held under spring pressure inside a coin cell. Before each experiment, cells were equilibrated at 120 °C for at least three hours. The batteries were cycled in a Maccor series 2000 battery-test system.

A JSM-6300 scanning microscope (Jeol Co.) equipped with a Link elemental analyzer and a silicon detector, was used to study surface topology. X-ray diffraction data were obtained with the use of a Θ-Θ Scintag powder diffractometer equipped with a Cu Kα source and a liquid-nitrogen germanium solid-state detector.

X-ray photoelectron (XPS) measurements of the pyrite cathodes were performed with a monochromatic Al Kα source (1486.6 eV) in UHV (2.5 x 10^{-10} torr pressure) with the use of a 5600 Multi-Technique System (Physical Electronics Inc., USA).

RESULTS AND DISCUSSION

Fig. 2 shows the SEM surface images (in the secondary-electron mode) of the cathodes prepared by doctor-blade technique (a, b) and RF sputtering (c, d). 1-10μm size particles have been distinguished on the surface of the composite cathode, while nano-size pyrite particles were found in the RFS (100% dense) cathode. Topographical images (obtained in the backscattered-electron mode) show full coverage of the surface of the current collector by pyrite for the cathodes prepared by both methods. Energy-dispersive X-ray analysis of the pyrite RF-sputtered cathode gives an Fe:S atomic concentration ratio close to 1:2, characteristic of the pyrite FeS_2 structure.
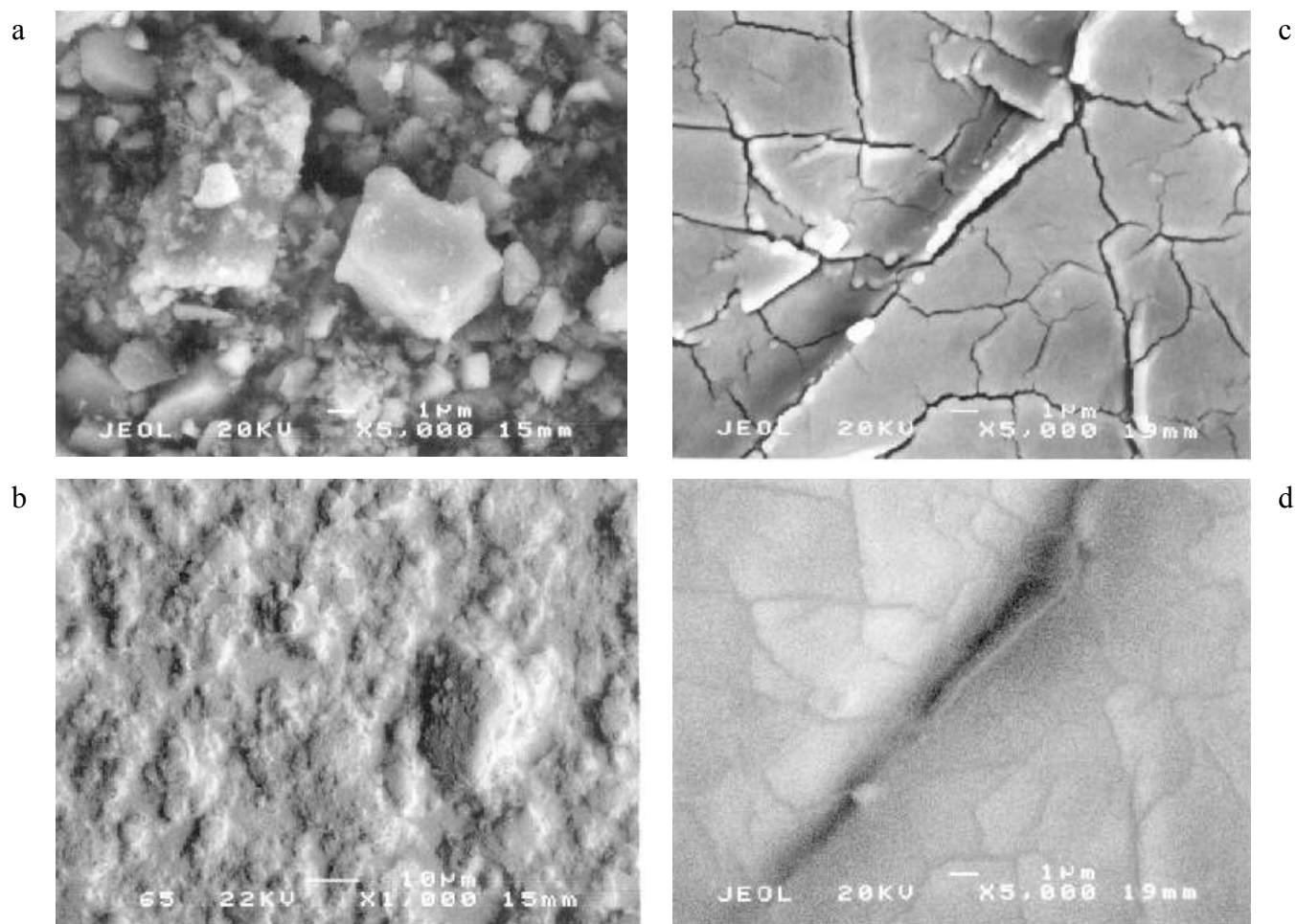
Fig. 2. SEM images of the surface of cathodes prepared by doctor-blade technique (a, b) and RF sputtering (c, d)

a, c-secondary-electron mode, b, d-backscattered-electron mode

In order to get more precise information on the composition of the RFS cathode, high-resolution XPS measurements were performed in the narrow window of 11.75eV with 0.05eV/step. The iron-

binding energy (Fe2p) region of the XPS spectrum of pyrite is shown in Fig. 3a. Two clear Fe2p peaks at 720 and 706 eV characteristic of pyrite [14] and a broad peak at about 711 eV of iron oxides and/or iron sulfates are detected. This peak, in addition, may also include the compound FeOOH with binding energy 711.3 to 711.8 eV [14]. The oxygen O1s signal at 532eV is typical of iron oxides (Fig.3b). The clear sulfur doublet at 162.4 and 163.6 eV in the S2p-XPS spectrum is related to pyrite, and the peak at 169 eV is attributed to the iron sulfates $Fe_2(SO_4)_3$ or $FeSO_4$ (Fig.3c). It should be mentioned that there are no XPS standards that enable the identification of sulfur deficiency in pyrite. Fitting of the S2p XPS spectrum was undertaken, therefore, with the use of the binding energy of FeS_2 and FeS (161.6eV). As a result, about 20 atomic percent sulfur deficiency in pyrite was found. This presumably can be related to the formation of either $0.8FeS_2/0.2FeS$ mixture, or $FeS_{1.8}$ (Fe_5S_9) structure.

After 2 minutes of argon sputtering, the relative atomic concentration of oxygen strongly decreases, indicating the absence of oxides in the bulk of the RFS cathode. The Fe:S atomic ratio does not change even after 10 minutes of sputtering. This points to the formation of a homogeneous sulfur-deficient structure in the RFS cathode.
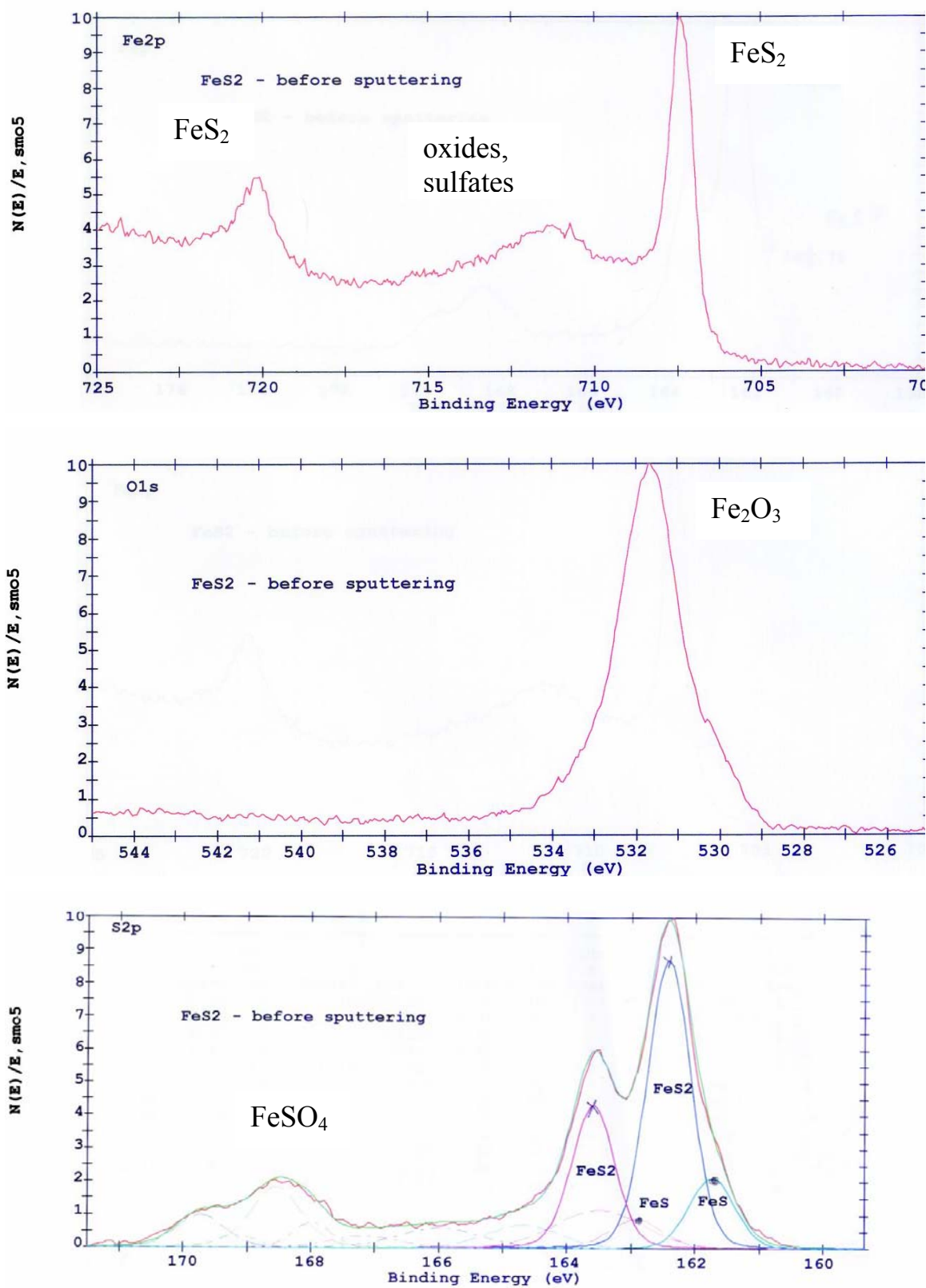
Fig.3. High-resolution XPS spectra of the RFS-pyrite cathode

As expected, the substrate on which sputtering is performed influences the final structure of the material. Pyrite sputtered on glass (Fig. 4a) is much more oriented than natural FeS_2 powder (Fig. 4b). A high-intensive [111] peak with lattice space 2.562A indicates formation of a strong texture with about 10-20nm grain size. This texture, while strong enough, is less pronounced when sputtering is performed on a graph-foil current collector. In the XRD pattern of the FeS_2-RF sputtered cathode both on the glass and graph foil, the main Bragg lines associated with pyrite were detected. In the pristine FeS_2 each iron atom is coordinated by six sulfur atoms, while sulfur bonds with three Fe and one S [15, 16]. The iron atoms are arranged in the face-centered cubic (fcc) sublattice in which the S atoms are imbedded, occupying positions along the (111) direction. The RFS pyrite was found to have an increased lattice parameter (5.4365A) as compared to that of powder obtained by milling of the target (5.4167A). This enlargement of the cell unit is not clear enough. It is assumed that RF sputtering is followed by the creation of sulfur defects and conversion of the octahedral sulfur arrangement to a disturbed tetragonal pyramidal symmetry with the FeS_5 molecule. In this coordination the d_{xz}, d_{xy} and d_{yz} orbitals are energetically more stabilized [15, 16], thus resulting in an additional state in the forbidden zone as a result of the sulfur deficit. In [15, 16] it was found that, even for the case of only 5% (atomic) sulfur deficiency, approximately 25% of the iron coordination would be affected as well. For about 20% sulfur deficiency, as in RFS pyrite, almost all the iron atoms would be disturbed. Therefore, by analogy with [15, 16], the electronic conductivity of the RFS pyrite is expected to be higher than that of the pristine material.
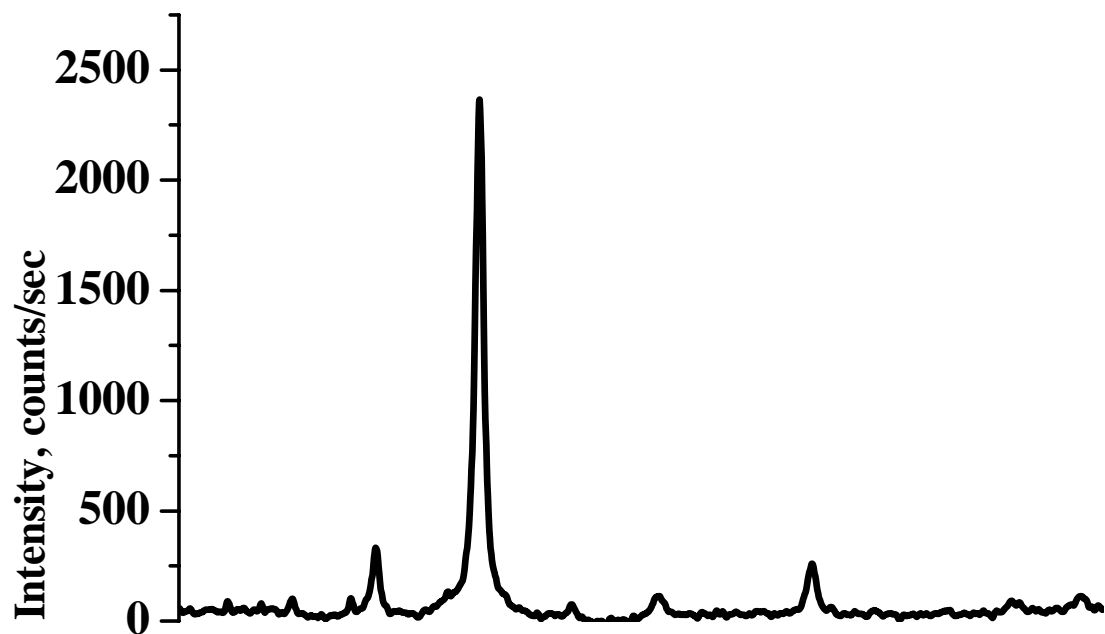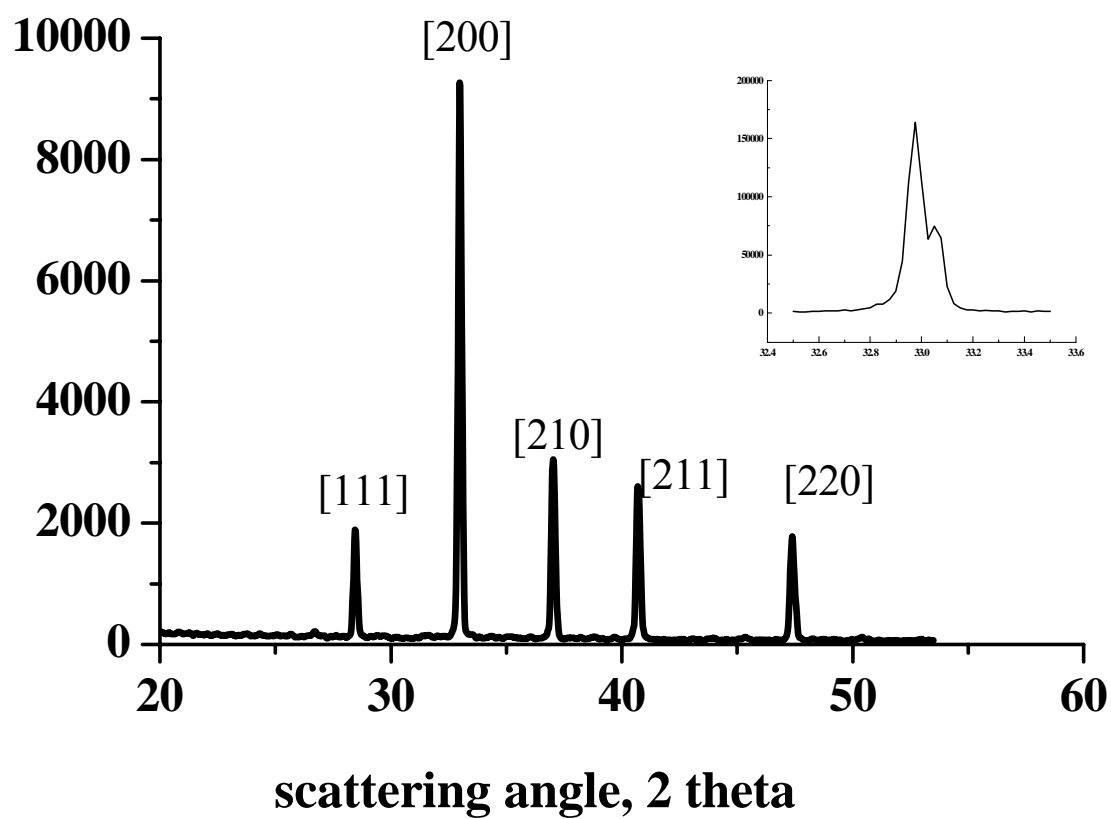
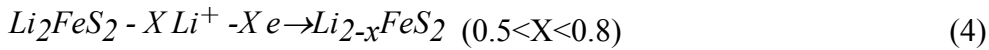Fig. 4. XRD patterns of the RFS pyrite (a) and milled target (b)

More than 50 cells with pyrite-based cathodes of different active-material content and thickness were constructed and cycled. Fig. 5 represents the first discharge curve of Li/CPE/pyrite cells with cathodes prepared by DB and RFS. For a Li/(CPE)/FeS$_2$ cell, the first discharge curve at 120 °C has two plateaus, one at about 1.8 V and another at 1.6 V. These are associated with the two-step reduction of FeS$_2$ (according to reactions 1 and 2):

$$FeS_2 + 2Li^+ + 2e \rightarrow Li_2FeS_2 \qquad (1)$$

$$Li_2FeS_2 + 2Li^+ + 2e \rightarrow Fe + 2Li_2S \qquad (2)$$

The high-voltage (2.4-1.8 V) shoulder appearing on the discharge curve may be attributed to the reduction of the partially oxidized cathode surface. This shoulder is more pronounced on discharge of the nano-size, roughly 1μm-thick RF-sputtered cathode. The overpotential of the first step of pyrite reduction is lower by 50 mV for the RF-sputtered cathodes. However, it is higher by 75 mV for the second step. This difference may indicate that Li$^+$ mobility is hampered in the Li$_2$FeS$_2$ phase in the absence of the CPE in the 100% dense cathode.

The first-cycle utilization of pyrite was found generally to be inversely proportional to the thickness of the DB-composite cathode and pyrite content. At low FeS$_2$ content (35%) the effect of thickness is less pronounced. Hot-pressing of cathodes results in a rise of FeS$_2$ utilization by 6 to 18%. Teflon-bonded cathodes showed 50% pyrite utilization. Utilization of pyrite during the first discharge in the ultra-thin RF-sputtered cathodes was the highest (88%).

Over the operating temperature of 120°C, pyrite is not regenerated on charge, therefore the discharge curves from the second cycle on differ from that of the first cycle. The simplified charge-discharge mechanism of pyrite in polymer electrolytes has been studied extensively [9, 11-13, 17, 18] and may be schematically described by the following reactions:
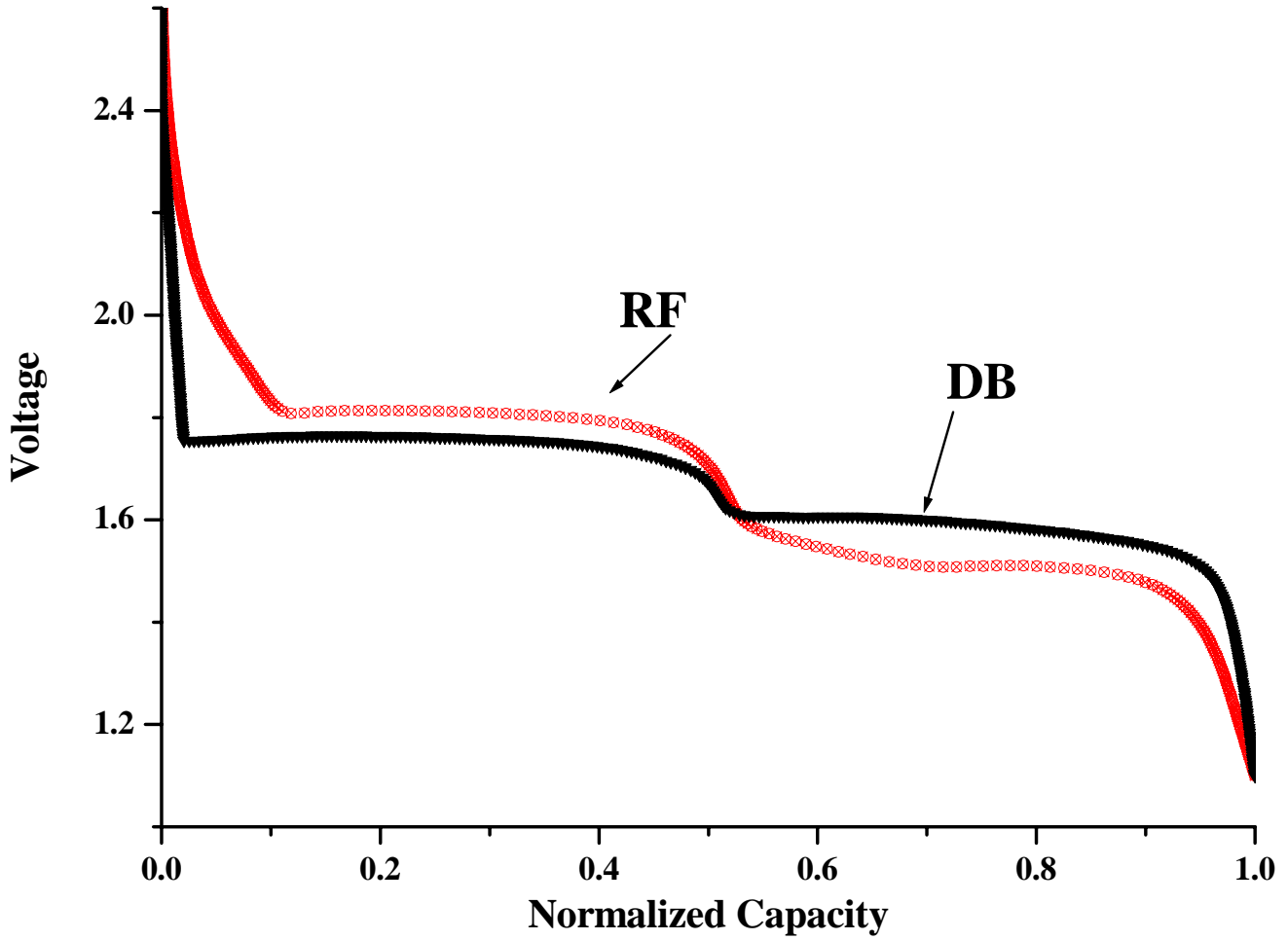
$$Fe + 2Li_2S - 2e \rightarrow Li_2FeS_2 + 2Li^+ \qquad (3)$$

$$Li_2FeS_2 - X Li^+ - X e \rightarrow Li_{2-x}FeS_2 \quad (0.5 < X < 0.8) \qquad (4)$$

Fig.5. First discharge of the Li/CPE/FeS$_2$ cells

CPE composition: LiI P(EO)$_{20}$ EC$_1$ 9% Al$_2$O$_3$

Operating conditions: T = 120 °C, i$_d$ = 0.05 mA/cm^2

cathode composition: DB-50% (v/v) FeS$_2$, 50% (v/v) CPE,

cathode thickness ,δ=10 μm

RFS-100% FeS$_2$, δ=1 μm

To get more precise information on the small changes occurring during charge-discharge, we carried out high-resolution voltage measurements. Four to seven phases have been identified and found to change during the first 30 – 50 cycles. These phases do not change much over the subsequent 400-500 cycles. Fig. 6 depicts the dQ/dV curves of the second charge-discharge cycle of cells composed of pyrite-based RFS and DB-composite cathodes. On the basis of on our previous studies, we associate

peaks B and C with reversible electrochemical reaction 3. The flat, high-voltage sections of the curves (1.9-2.2 V on charge and 1.75-2.1 on discharge) are attributed to the reversible insertion/deinsertion of lithium to/from the Li_2FeS_2 host, complicated by a phase change (peaks D and A). This phase transition is more pronounced in the case of cathodes composed of natural pyrite. Deinsertion of lithium results in the oxidation of iron (II) to iron (III), the process being accompanied by a change in iron-ion occupancy from tetrahedral to octahedral at an advanced stage of the reaction [7, 19]. Peak D, therefore, is likely to be related to the shift of iron atoms from tetrahedral to octahedral coordination. It has been recently found [17, 20] that pyrolysis of pyrite is followed by a 100mV decrease in the charge overpotential. This was explained by the formation of tetrahedral sulfur vacancies in the Li_2FeS_2 phase, which may be occupied by iron ions. Strong depression of peak D in the dQ/dV curves of the lithium cells with RFS cathodes may therefore be related to the formation of a sulfur-vacancy-rich structure, similar to that formed on pyrolysis,. This structure has increased lattice space detected by XRD and XPS methods. This is in agreement with data presented by Blandeau et al [19], who showed that in Li_2FeS_2 the Fe-S interatomic distance for the main (FeS_4) tetrahedra is 2.357Å. For the surrounding octahedra the Fe-S distance is 2.53 Å. Such structure is expected to permit greater mobility of iron, which, in turn, favors the tetrahedral to octahedral iron shift. In addition, a low S/Fe ratio in the FeS_2 lattice was followed by enhanced electronic conductivity of the material [21], thus decreasing the IR drop and probably increasing the diffusion coefficients of Li^+, Fe^{2+} and Fe^{3+}. Low charge/discharge overpotential of the lithium cells with RFS cathodes (Fig. 6) is good evidence of increased electronic conductivity of the sputtered pyrite.
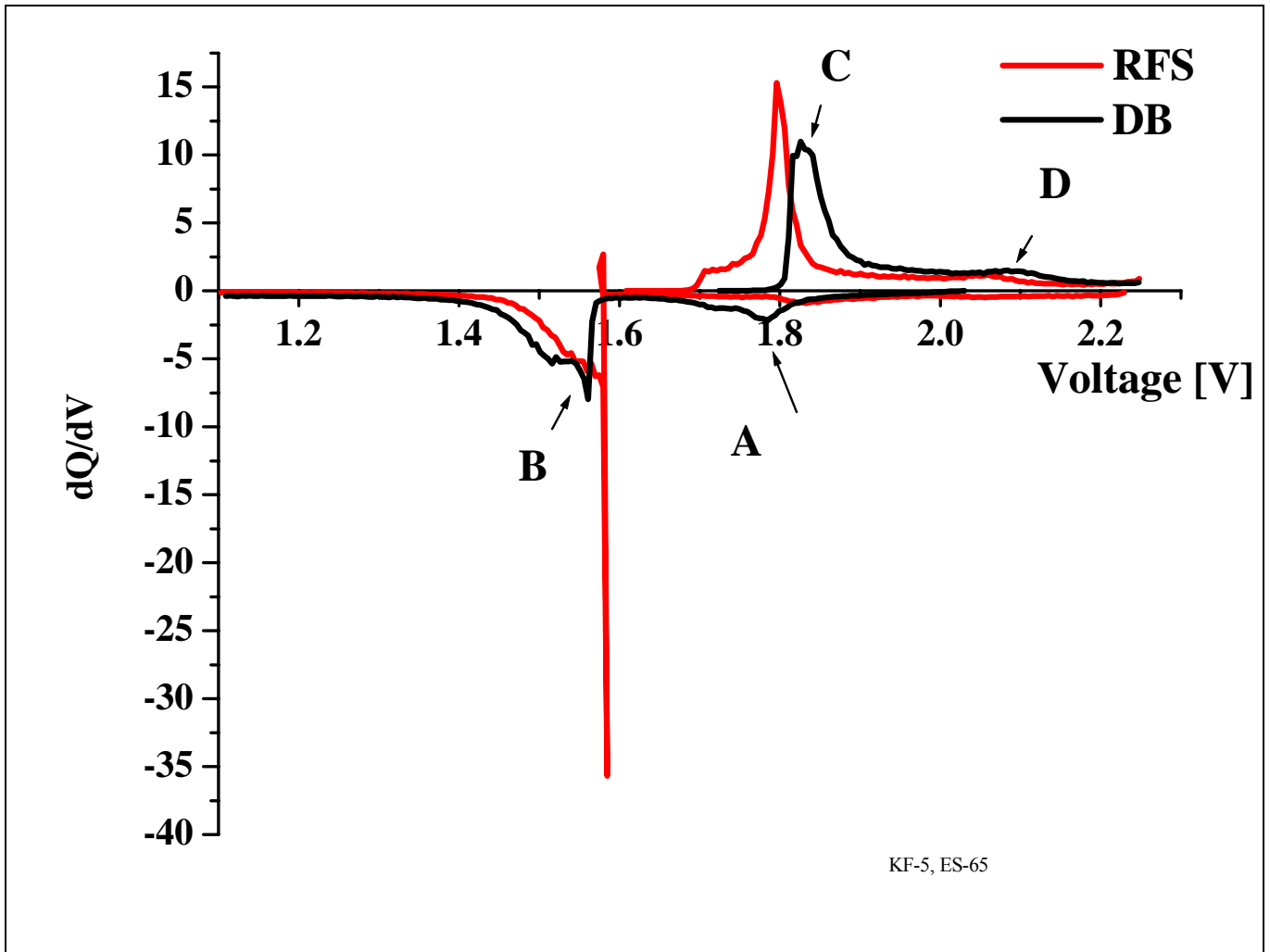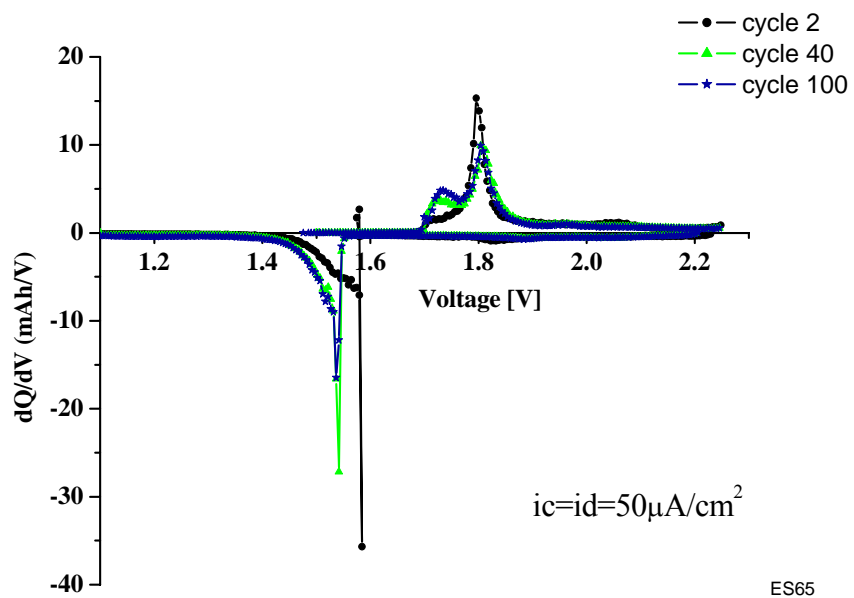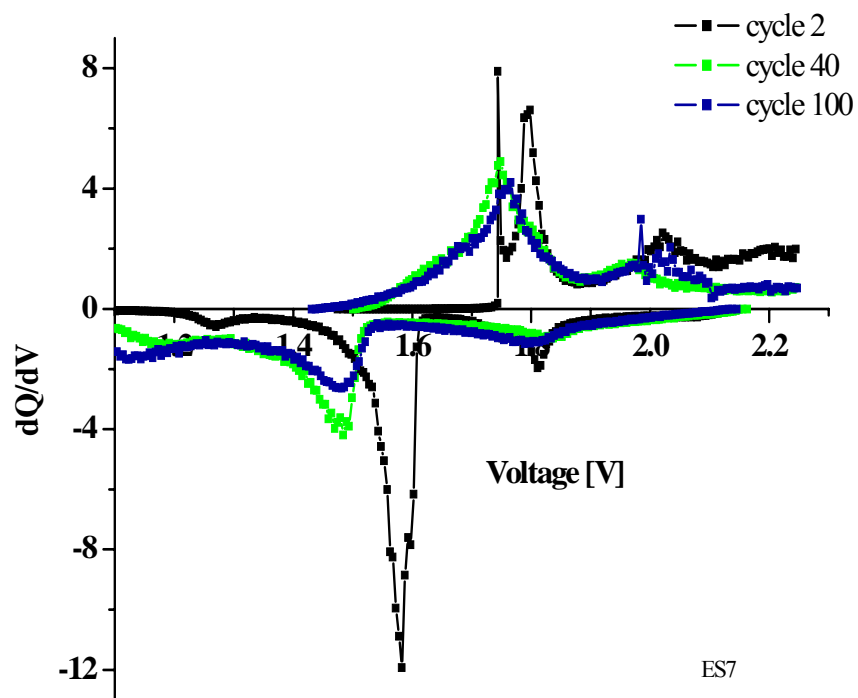
Fig. 6. dQ/dV curves of the of the second cycle of the Li/CPE/FeS$_2$ cells with RFS and DB cathodes Operating conditions: T = 125 °C, $i_d = i_{ch} = 0.05$ mA/cm^2

Fig. 7 shows dQ/dV curves of long-term cycling of the Li/CPE/FeS$_2$ cells with different cathodes. In the cells with both RFS, cast and DB composite pyrite CPE-bonded cathodes, the maximum of the discharge peak B shifts to lower cell voltages by about 40mV. Also, on further cycling up to about cycle 20-30, an additional shoulder develops. The amount of the generated phase increases, but the position of the peak does not change much over the subsequent 100 cycles, indicating the attainment of the phase steady state in the cathode. At high discharge current density (300µA/cm^2, c/3) peak B in the discharge curves of the cells with composite cathodes gradually shifts toward lower voltage by 70 to 100mV. We believe that this phenomenon may be due to the transport limitations of Fe^{2+} in Li$_2$FeS$_2$ followed by the occurrence of an ion-transport barrier similar to that of the limiting current

phenomenon. For RFS cathodes, however, increase of the discharge rate from c/7.5 to c/1.8 does not affect the long-term discharge overpotential.

Long-term cycling of the cells with Teflon-bonded cathodes (Fig. 7d) is followed by intensive build-up of discharge overpotential. This is possibly due to the increased mass- transport limitations and the IR drop as a result of the negligible Li^+ conductivity of Teflon and loss of contact between active cathode material particles. At the end of the second and all subsequent discharges, the fractional change in the cathode active material volume is about +27%. On charge, the cathode contracts by about 21% [12]. It seems likely that the Teflon used as a binder in composite pyrite-based cathodes does not sufficiently prevent the separation of cathode-active material particles.

At deep discharge (down to 1.1V) of the lithium/composite polymer electrolyte/pyrite battery an additional plateau forms at about 1.3V. It is noteworthy that in the dQ/dV curves of the Li/FeS_2 cells with cast cathodes this plateau appears as a pronounced peak (Fig. 7b); for the cathodes prepared by the DB technique, the increased contribution of low-voltage reactions emerges as progressively increased area below the zero dQ/dV level (Fig.7c). In our previous work [12], we suggested that several parallel, undesirable reactions might take place resulting in the formation of an additional phase. It is now well established by powder X-ray diffraction (PXRD), Near-Edge X-ray Absorption Spectroscopy (NEXAS) and Mossbauer spectroscopy [10, 18, 22, 23], that the final product of fully reduced pyrite is supermagnetic iron in the form of atoms or small (about 3.6nm) aggregates of atoms. These are highly active and have a large surface area. Such a cathode surface becomes highly susceptible to attack by the electrolyte components, which comprise 20 to 65% (v/v) of the composite cathode. Partial decomposition of the electrolyte and the formation of undesirable products bear out the electrochemical incompatibility of nano-size iron particles and CPE. Although the electrochemical reactions are reversible, they decrease the total operating voltage and increase capacity loss of the battery. The low-voltage plateau appearing as a broad peak in the high-resolution dQ/dV discharge curves of the Li/pyrite cells with RFS cathodes (Fig. 7a) is scarcely visible even in the enlarged 1.1-1.5 V region. However, the gradual development of the 1.6 V shoulder on charge may indicate that, while less pronounced, there is the formation of the low-voltage phase. The absence of the CPE as binder in the RFS cathode may explain the depression of the dQ/dV peak at 1.2-1.3 V. Therefore the high reactivity of nano-size iron particles towards CPE cannot be excluded. To clarify the composition of the 1.3V phase, synchrotron x-ray absorption measurements were performed on a series of cells cycled more than 100 times. The results will be presented in a forthcoming publication.
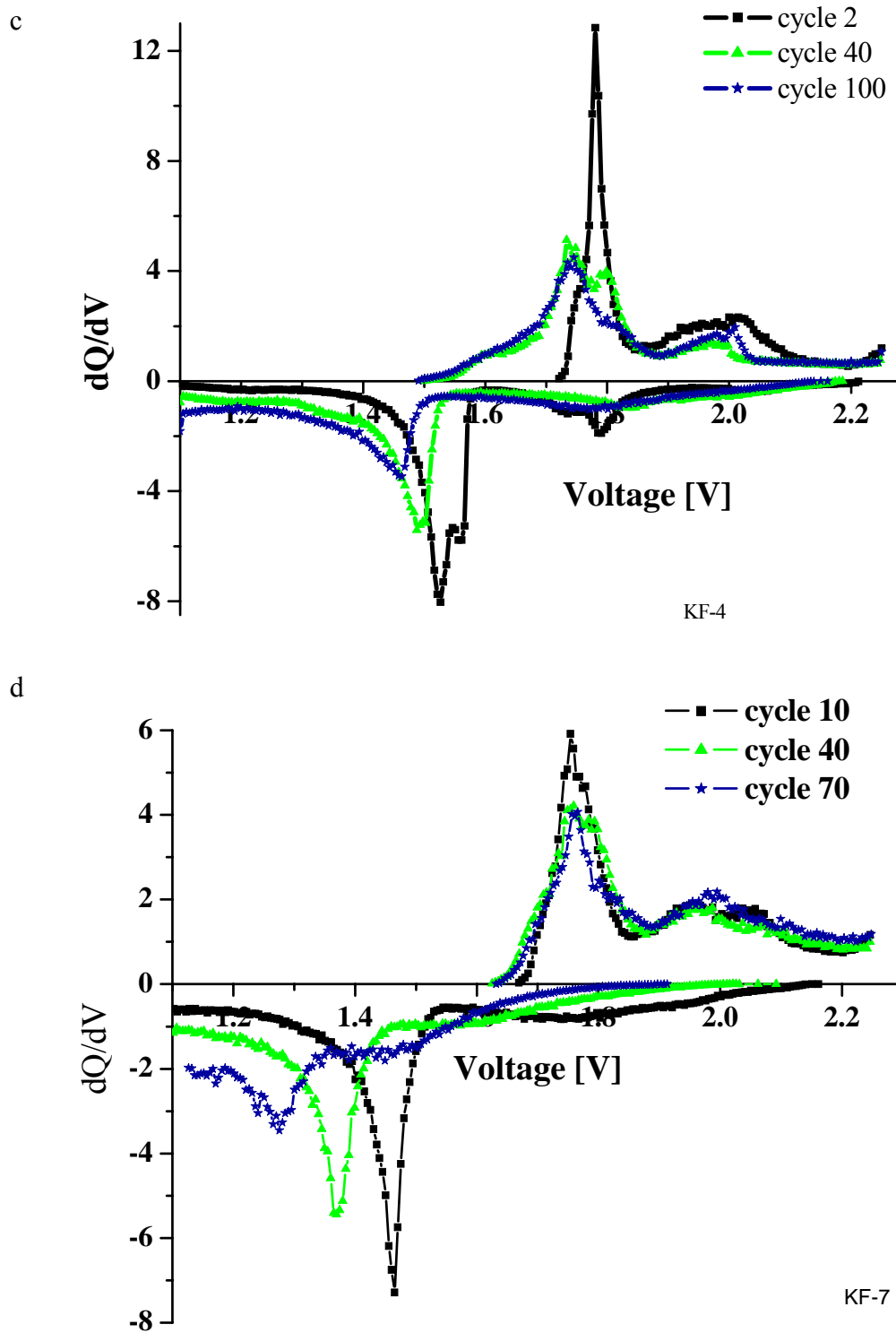
a

b

c

d

Fig. 7. dQ/dV curves of the long-term cycling of the Li/CPE/FeS$_2$ cells with different cathodes: a) RFS*; b) CPE-bonded cast; c)CPE-bonded DB; d) Teflon-bonded DB,

Operating conditions: T = 125 °C, i$_d$ = 0.05 mA/cm^2, i$_{ch}$= 0.3 mA/cm^2.

* i$_d$ =i$_{ch}$= 0.05 mA/cm^2

Fig. 8 shows the plots of capacity loss and charging efficiency of the Li/CPE/pyrite cells with RFS and DB cathodes. It is clear that the main capacity loss of all the cells occurs during the first 30 cycles (0.4-0.5%/cycle). On subsequent cycling, the degree of degradation decreases to 0.1-0.15 %/cycle. The Faradaic efficiency increases respectively from 90 to 96%. This coincides with the attainment of the phase steady state in the cathode. The capacity loss in the cells with cast, DB and CPE-bonded composite cathodes and Teflon-bonded cathodes is 0.2-0.4%/cycle at i_d= 300μA/cm^2 (c/3.3) and i_c=50 μA/cm^2 (c/20).
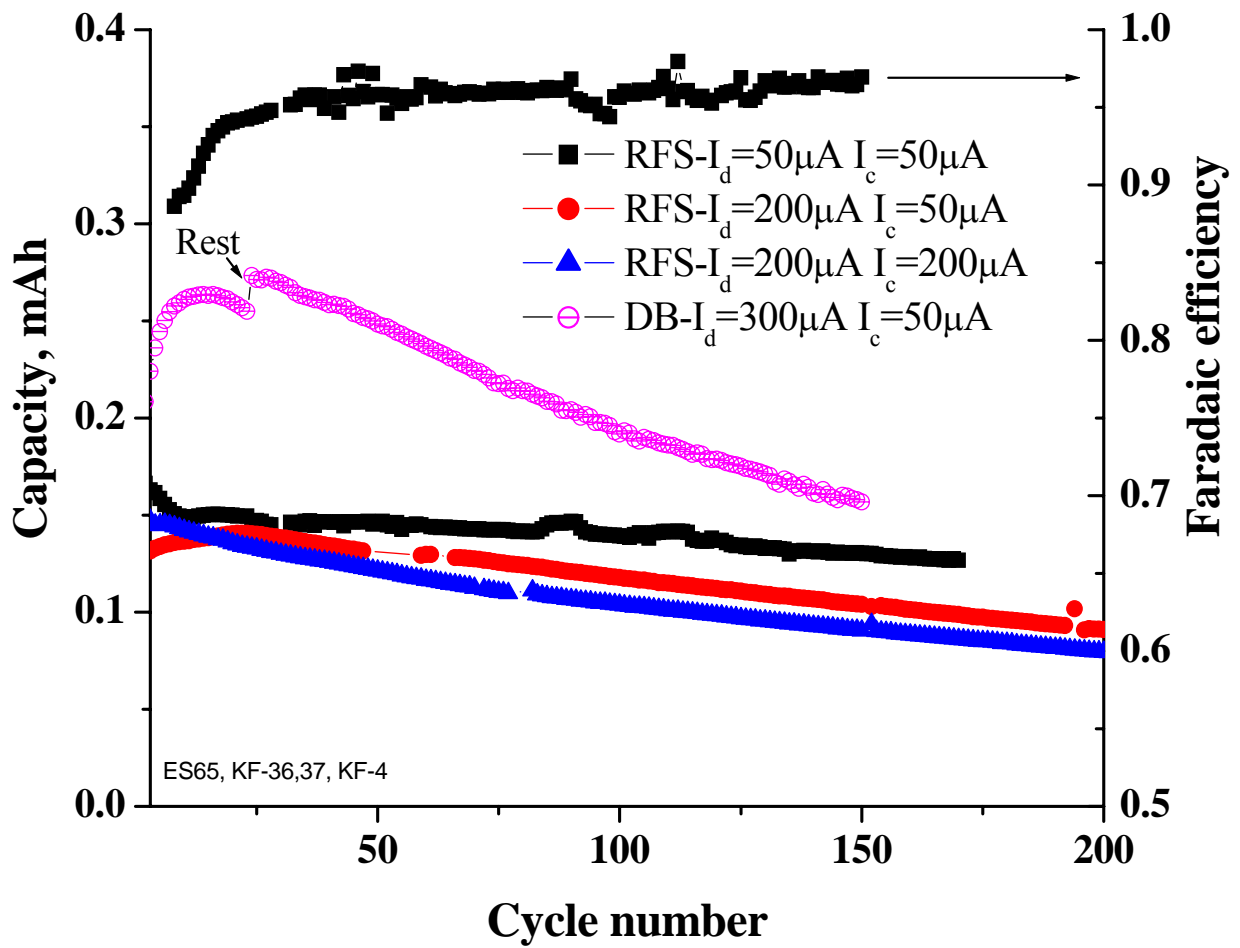
Fig.8. Plots of discharge capacity and Faradaic efficiency vs. cycle number

In order to prevent undesirable reactions from occurring at deep discharge and to achieve long-term stability of the CPE-containing composite cathodes (similar to that of the Li/FeS$_2$ cells with RFS cathodes), the procedure of the formation of cathode SEI was developed [12, 24]. This is based on the overdischarging of the Li/FeS$_2$ cells during several cycles. The cathode SEI increases compatibility of the CPE with atomic iron and, as a result, decreases the long-term degree of degradation of the Li/CPE/pyrite cells to 0.1%/cycle.

We would like to emphasize that there is almost no change in the capacity loss with increase in charge-current density up to c/1.8 in Li/CPE/pyrite cells with RFS cathodes. For the cells with cathodes composed of natural pyrite and bonded with CPE, the degradation rate for the same operating conditions increases up to 0.5-0.8%/cycle. We believe that our experimental findings show considerable promise for the creation of sulfur-deficient pyrite structures for cathodes to be used in high-energy-density all-solid-state lithium batteries.

ELECTRODEPOSITED CATHODES

Experimental

The iron-sulfide films were electrodeposited galvanostatically on nickel substrates with the use of a conventional two-electrode cell with a graphite counter electrode. According to several reports [3-7], electrodeposition of iron sulfide is performed from solutions of $FeSO_4$. However, solutions of ferrous iron are unstable, since Fe^{2+} readily oxidizes to Fe^{3+}, which readily precipitates as iron (III) hydroxide at pH higher than 4. The electroplating bath used in this work contained: 0.01M $Fe_2(SO_4)_3$, 0.3M $Na_2S_2O_3$, and some additives. The temperature of the bath was 50°C, the current density i=1-10 mA/cm^2, pH 3.5-4.0 was adjusted by addition of H_2SO_4. All solutions were prepared from analytical-grade chemicals dissolved in deionized water. The thickness of the deposits was measured by an α-stepper (Dektak 3).

As-deposited samples of thin-film FeS cathodes were dried under vacuum at about 100 $^\circ$C for 6 hours. All subsequent handling of these materials took place under an argon atmosphere in a VAC glove box containing less than 10 ppm water. The electrochemical coin cells (type 2032) comprising a 0.95 cm^2 lithium anode, $LiI_1P(EO)_{20}EC$, 12% (v/v) Al_2O_3 composite polymer electrolyte (CPE) and a deposited cathode were constructed and cycled in a Maccor series 2000 battery-test system.

Results and Discussion

When thiosulfate is added to $Fe_2(SO_4)_3$, reduction of Fe^{3+} to Fe^{2+} occurs (reaction 1). At the same time, the thiosulfate ion decomposes to colloidal sulfur and HSO_3^- (aq) in the acidic medium (reaction 2). The formation of sulfur is evident from the turbidity of the solution [8]. During the reduction of sulfur in the presence of the iron (II) ions, the iron sulfide film is formed according to reaction 3, once the solubility-product constant is reached. The formation of H_2S (reaction 4) and its subsequent interaction with Fe^{2+} (reaction 5) cannot be excluded, either.

$$2Fe^{3+} + 2S_2O_3^{2-} \rightarrow 2Fe^{2+} + S_4O_6^{2-} \tag{1}$$

$$H^+ + S_2O_3^{2-} \rightarrow S_{(colloidal)} + HSO_3^- \ (aq) \tag{2}$$

$$Fe^{2+} + (1+x)S + 2e^- \rightarrow FeS_{1+x} \tag{3}$$

$$S + 2H^+ + 2e^- \rightarrow H_2S \tag{4}$$

$$Fe^{2+} + (1+x)H_2S \rightarrow FeS_{1+x} + 2(1+x)H^+ \tag{5}$$

The electrodeposition of iron sulfides was carried out for 5, 10, 15 and 30 min. During the experiment, a black deposit formed on the electrode. The thickness of the deposit varied from 0.3 to 1.2 μm. Thin films with smooth and uniform morphology were deposited at current densities of 1 to 5mA/cm^2. Above this current density, internal stresses develop in the deposit and this is followed by its disintegration and separation from the base. Poor adhesion of the deposit to the nickel substrate was also observed when the thickness was greater than 1.5 μm.

The surface morphology of the deposits varied slightly with current density. From the SEM micrographs (Fig. 9, insert) it is seen that iron sulfide deposits at low current density are made up of closely packed units of several square micron areas. Each unit has a porous network-like structure. In the SEM images of the films obtained at high current density, individual grains cannot be distinguished. The films obtained at 5mA/cm^2 show less compact bulk morphology (Fig. 9) and have a porous, sponge-like structure. It is noteworthy that the morphology of the coatings depends on the deposition time. Grain size appears to be inversely proportional to deposition time. This could be due to high internal stresses that develop during deposition and cause intragrain destruction. From the EDS measurements it was found that the Fe:S atomic ratio varies with deposition time from 1:1.4 to 1:1.1.

No visible Bragg lines of the crystalline iron sulfide or iron disulfide phase are detected by XRD and this indicates that the sub- and few-micron-thick FeS_x films are amorphous.

High-resolution XPS spectra of the as-deposited samples at different sputtering times were recorded. Two broad Fe2p doublets with maximums at about 707, 710, 720 and 724eV are associated with both iron mono- and disulfide. The peaks of iron oxides, however, fall in the same binding-energy region (708.1- 711.6 eV). The broad peaks, in addition, may include those for FeOOH with binding energy 711.3 to 711.8 eV. Two oxygen O1s structures at 529.9 and 531.6eV, observed on the surface of the deposit, are typical of iron (II) and iron (III) oxides. After 2 minutes of sputtering, the intensity of the high-energy signal (531.6eV) decreases sharply, but the corresponding shoulder still exists after 12 minutes of sputtering, indicating the presence of oxides in the bulk. In addition, sputtering results in overlap of two nearby Fe2p peaks and their shift toward lower energies. The shift reflects the higher concentration of the FeO in the bulk of the deposit, in agreement with the decreased bulk concentration of oxygen (from 29.9 to 13.6 atomic percent after 12 minutes of sputtering). A broad XPS band with a sharp maximum at 161.7 eV and two shoulders at 161.3 and 162.9 eV, are seen in the S2p spectra of the deposit (Fig. 10, 0 time of sputtering). From the fit of the S2p spectrum with standard spectra of compounds containing Fe-S bonds, it was deduced that there are at least three iron sulfide phases in the deposit. The first one is FeS_2, the second is iron monosulfide and the third, a non-stoichiometric FeS_{1+x} compound. The atomic concentration ratio: $FeS_2/(FeS + FeS_{1+x})$ is 1:4. Sputtering results in an increase in the intensity of the 161.7 eV band, but even after 12 minutes of sputtering, the concentration ratio does not change. $FeSO_4$ and $Fe_2(SO_4)_3$ are not found in the deposit, as indicated by the absence of the corresponding bands at around 168.7-169.1 eV.

The first discharge of $Li/CPE/FeS_x$ cells is represented by one well defined plateau at 1.53V and differs from the discharge of cells with RF-sputtered non-stoichiometric binder-free FeS_{2-x} cathodes [9]. It also differs from the discharge of cells with composite FeS_2-based cathodes, where two plateaus at 1.8V and 1.6V appeared. The final products of full discharge in both cells are metallic iron and Li_2S. As can be seen from the dQ/dV curves (Fig. 11), the kinetics of charge-discharge processes does not change significantly on cycling. One strong dQ/dV discharge peak is observed at 1.54 V. This corresponds to the charge peak at 1.8 V. The charge/discharge overpotential (half distance between the peaks), which is about 130 mV, does not vary on prolonged cycling of the Li/CPE cell containing an electrodeposited iron sulfide cathode. The appearance of the 1.9 V charging dQ/dV peak, with a slightly pronounced shoulder on the cathode branch of the curve, may be associated with phase

transition in the mixture of FeS_x compounds. It will be noted that the ratios between the integral capacities of the dQ/dV peaks at 1.8 and 1.9 V and the widths of the peaks are different in the cells with iron sulfide cathodes deposited at different sputtering times. That is, in the lithium cells with iron sulfide cathodes that are a few microns thick, the peak at 1.9 V is 1.5 to 2 times more intensive than that at 1.8 V. However, in the cells with submicron-thick cathodes, the reverse is true. This difference is possibly caused by different Fe:S ratios and FeS_x phases of the deposit.

On the basis of the electrochemical experimental data we suggest, that at the first charge step two-electron oxidation of metallic iron to FeS occurs. This is followed by the formation of a highly disordered, possibly amorphous, form of pyrrhotite, $Fe_{1-\delta}S$, with Li^+ balancing the charge. On the other hand, the position of the main dQ/dV peaks appearing on reversible cycling of Li/solid composite polymer electrolyte/pyrite cell almost coincide with those of the cells composed of electrodeposited non-stoichiometric iron sulfide cathodes. Therefore, the mechanism ascribed to the FeS_2-based lithium cells cannot be ruled out either. According to this mechanism, the oxidation of metallic iron proceeds via the formation of Li_2FeS_2 attended by partial deintercalation of lithium with $Li_{2-x}FeS_2$ ($0.5<x<0.8$) as the final product. In our previous work (see above) a two-voltage-step lithium reaction mechanism at ambient temperature Li/FeS_2 cells was proposed. It was shown that a crystalline, layered $Li_{2+x}Fe_{1-x}S_2$ ($0.33 \geq x \geq 0$) equiaxed grain intermediate phase was produced from the first lithium reduction. In order to clarify the composition of intermediates formed on cycling of $Li/CPE/FeS_x$ cells with electrodeposited cathodes, phase synchrotron x-ray absorption measurements will be carried out. The results will be presented in a forthcoming publication.

The $Li/CPE/FeS_x$ cells showed stable and reversible electrochemical behavior. For over 650 cycles the capacity loss of these cells, charged/discharged at C/1, was not more than 0.06%/cycle at 100% DOD (Fig. 12).
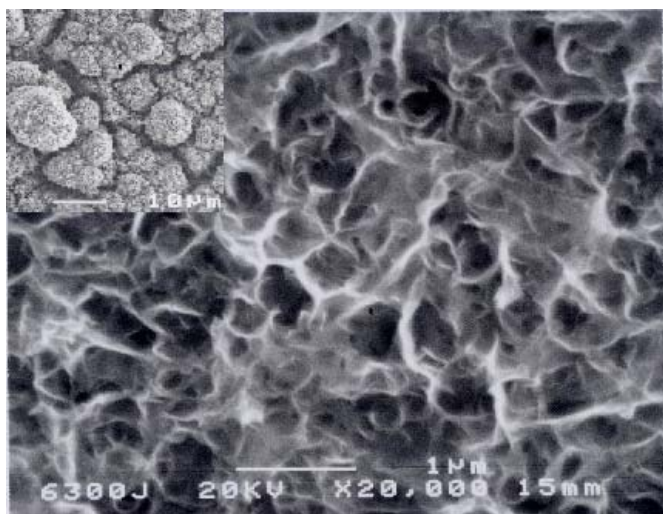
Fig. 9. SEM micrograph of the electrodeposited FeS$_x$ cathode (insert-deposit at low current density)
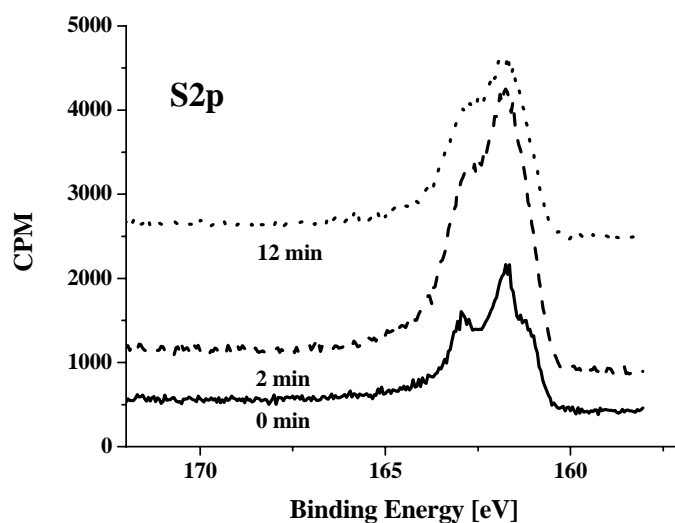
Fig. 10. S2p XPS spectra of the electrodeposited iron sulfide cathode
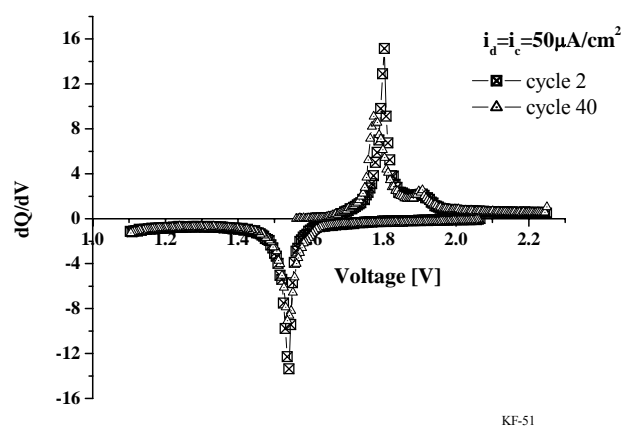
Fig. 11. dQ/dV charge/discharge curves of Li/CPE/FeS$_x$ cell

CPE composition: LiI P(EO)$_{20}$ EC$_1$ 9% Al$_2$O$_3$

Operation conditions: T = 125 °C, $i_{ch}=i_d=50\mu A/cm^2$
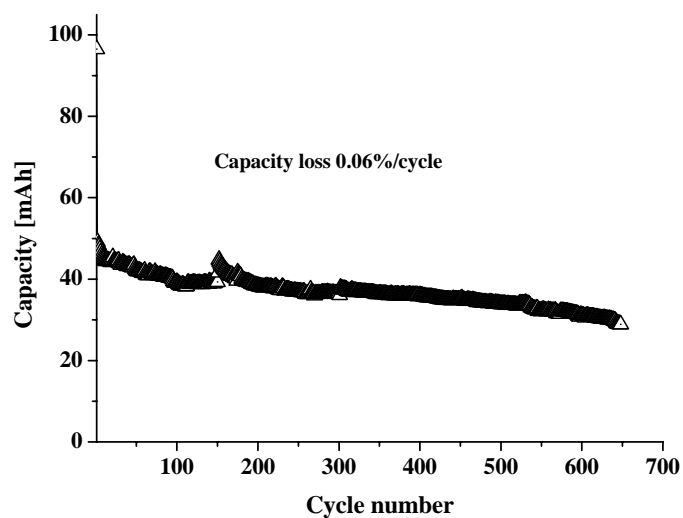
Fig. 12. Cycle life of the Li/CPE/FeS$_X$ cell, $i_{ch}=i_d=50\mu A/cm^2$, T=125°C

References

1. J.B.Bates, N.J.Dudney, G.R. Gruzalski et. A., J.Power Sources, 43 (1993) 127

2. Z. Tomczuk, B. Tani, N. C. Otto, M. F. Roche, and D. R. Vissers, *J. Electrochem. Soc.*, 129, 926 (1982)

3. J.C. Nardi, M.B. Clark, W.P. Evans. Symposium on Electric Power Sources in Horological and Microtechnical Protection, Mulhause, France, Extended Abstracts, 48, (1981)

4. C. Iwakura, N. Isobe, H. Tamura, *Electrochimica Acta*, 277, 126, (1983)

5. H. Ikeda, S. Narukawa, S. Nakaido. *21st Battery Symposium in Japan*, Okayama, Extended Abstracts, p 47, (1980)

6. K. Hansen, K. West. *Electrochemical Society Proceedings*, 97-18, 124 (1997)

7. R. Brec, E. Prouzet and G. Ouvrard, *J. Power Sources*, 26, 325 (1989).

8. P.Gard, C.Sourisseau, G. Ouvrard, R.Brec, *Solid State Ionics*, 20, 231 (1986)

9. D. A. Scherson , *The Electrochemical Society Interface*, Fall, 34 (1996)

10. R. Fong, J.R.Dahn and C.H.W.Jones, *J. Electrochem. Soc.*, 136, 11, 3206 (1989)

11. E. Peled, D. Golodnitsky, G. .Ardel, J. Lang and Y. Lavi , *J. Power Sources*, 54, 496 (1995).

12. E. Strauss, D. Golodnitsky, and E. Peled, *Electrochimica Acta*, 45, 8-9, 1519 (2000)

13. E. Strauss, D. Golodnitsky, and E. Peled, S. Kostov, D.Garan, M. denBoer and S. Greenbaum, *J. Power Sources*, 81-82, 715 (1999)

14. Handbook of X-ray Photoelectron Spectroscopy, Ed.:J. Chastain, Perkin-Elmer Corp., USA, 1992

15. A. Ennaoui, S. Fiechter, Ch. Pettenkofer, N. Alonso-Vante, K. Buker, M. Bronold, Ch. Hopfner, H. Tribusch, Solar Energy Materials and Solar Cells, 29, 289, (1993)

16. M. Birkholz, S. Fiechter, A. Hartmann, and H. Tributsch. *Physical Review B*, 43,14, 11926, (1991)

17. E. Strauss, D. Golodnitsky, and E. Peled. *J. Solid State Electrochemistry*, 6, 468-474 (2002)

18. D. A. Totir, I. T. .Bae, Y. Hu, Y. Gofer, Y. .Mo and D. A. Scherson, *Proceedings of the Symposium on Lithium Polymer Batteries*, 96 - 17, 269, (1996)

19. L. Blandeau, G. Ouvrard, Y. Calage, R. Brec, J. Rouxel. *Journal of Physics C: Solid State Physics*, 20, 27, 4271 (1987)

20. D Golodnitsky, E. Peled, *Electrochimica Acta*, 1-2, 45 335 (1999)

21. C. de las Heras, G. Lifante, J. Applied Physics 82,10, 5132 (1997)

22. K. Takada, Y. Kitami, T. Inada, A. Kajiyama, M. Kouguchi, S. Kondo, M. Watanabe, M. Tabuchi. *J. Electrochem. Soc.*, 148, 10, A 1085-1090 (2001)

23. D. A. Totir, M.R. Antonio, P. Schilling, R. Tittsworth, D. A. Scherson, *Electrochimica Acta*, 47, 3195 (2002)

24. E. Strauss, D. Golodnitsky, and E. Peled. *Electrochemical and Solid-State Letters*, 2 (3), 115 (1999)

PART 2. DEVELOPMENT AND CHARACTERIZATION OF SINGLE-LITHIUM-CONDUCTING POLYMER ELECTROLYTES

Much effort has been applied to the development of highly conductive, chemically and mechanically stable solid polymer electrolytes (PE) because of their possible applications in electrochemical devices, such as fuel cells, memory devices and "smart windows". These materials are formed by dissolving a salt (for example LiI) in a solid host polymer such as poly(ethylene oxide). However, the need to operate PE-based devices at temperatures well above ambient has severely restricted their application. In addition, for most state-of-the-art PEs, the lithium-ion transference number (t_+) is less than unity. The anionic mobility results in the formation of an undesirable salt-concentration gradient and causes a very substantial addition to the voltage across a polymer electrolyte at constant-current operation. This degrades the performance of the batteries and therefore the synthesis of single-cation-conductive flexible polymer electrolytes is considered of prime importance. In order to obtain a single-cation-conducting system the counter ions must be sufficiently large or chemically attached to the polymer backbone as in the case of typical polyelectrolytes.

CHARACTERIZATION OF POLYMER-IN-SALT ELECTROLYTES
Experimental

Preparation of polymer-in-salt electrolyte

On dissolving the crystalline $LiAlCl_4$:PAAM (1.5:1) sample in acetonitrile, both at room temperature and on heating up to 50ºC, a homogeneous suspension is formed. The resulting film (after evaporation of solvent) was found to be extremely brittle and completely unusable for the solid-electrolyte application. In order to test this material as a solid electrolyte, the crystalline particles were ground to a powder and mixed with ethylene carbonate (10% w/w). EC was added as a good plasticizer in order to improve the conductivity and interfacial properties of lithium. Pellets of about 1mm thickness were formed in the "Macro-micro KBR Die" under a pressure of 5 tons at room temperature.

A solid polymer electrolyte (SPE) based on the co-polymer of 67.8 mol% of acrylonitrile with 32.2 mol% butyl acrylate and 72 w/w % (stoichiometrically with respect to AN) of $LiN(CF_3SO_2)_2$ was used as received from Warsaw University. To separate the film from the glass support it was vacuum-dried at room temperature.

Fig. 2.1. shows the SEM images of a $LiAlCl_4$:PAAM electrolyte prepared by hot pressing. Deep cracks, observed in the micrographs were not through cracks, however. Surface mapping showed homogeneous distribution of the elements.

The DSC thermograms of the initial powder and electrolyte in the form of a pellet are presented in Fig.2.2. Three phase transitions were detected in the DSC traces of both samples. Two small endotherms in the vicinity of 85 and 130 °C might be attributed to softening of the material. A strong exotherm at $220\ ^0C$ is associated with the decomposition of the solid compound A clear shift of this endothermic peak to higher temperature and decrease of its enthalpy value is observed in the DSC trace of the SIC disc, thus indicating higher thermal stability.

A Nyquist plot of the symmetrical Li/SIC/Li cell is represented by a single, highly depressed semicircle (Fig. 2.3.). The total impedance of this arc is in the range of 50 Mohm. It should be emphasized that at temperatures below $90\ ^0C$ AC tests were physically unfeasible. Another interesting observation is that increase of the temperature from 90 to $125\ ^0C$ does not significantly influence the ionic conductivity (Fig. 2.4.). At temperatures above $130\ ^0C$ the release of some volatile component

from the electrolyte was observed (in agreement with the DSC measurements). This is followed by strong passivation of lithium.
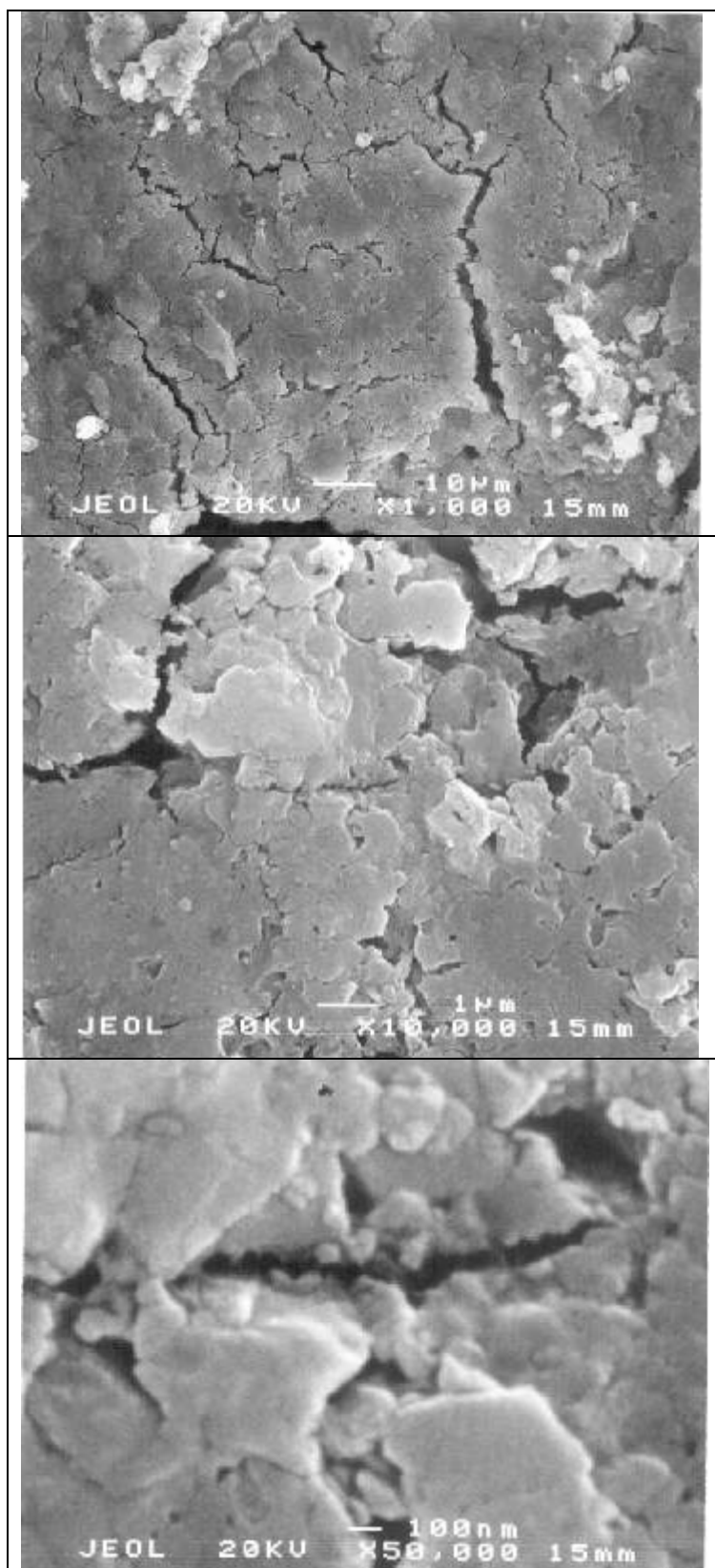
Fig. 2.1. SEM images of a pellet of the LiAlCl$_4$:PAAM:EC (1.5:1:1) SIC
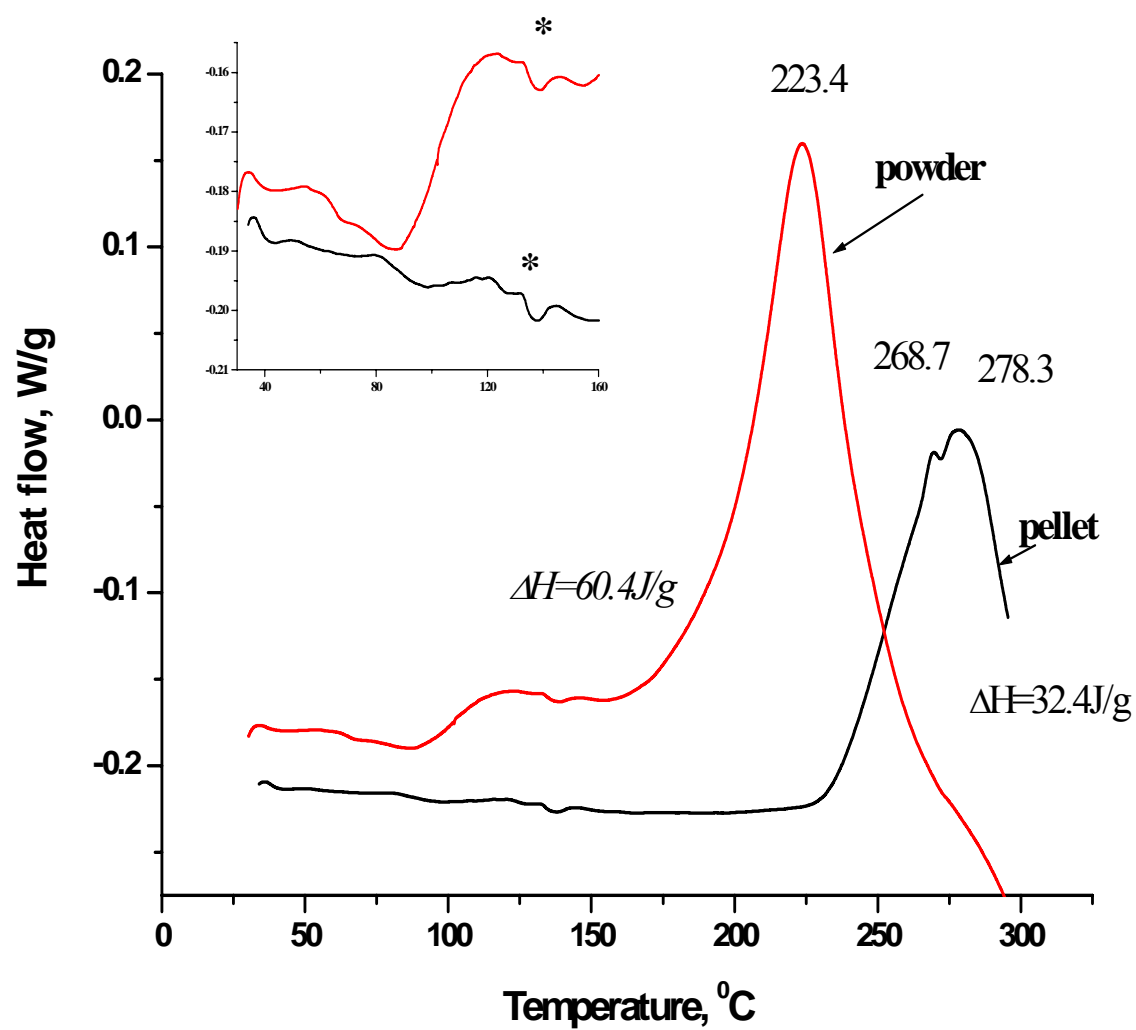
Fig 2.2. DSC thermograms of pristine powder and SIC pellet

	Tp$_1$ ^{0}C endo	Tp$_2$ ^{0}C endo	Tp$_3$ ^{0}C exo	ΔH$_1$ J/g	ΔH$_2$ J/g	ΔH$_3$ J/g
powder	89	137	223	2.3	0.13	60.4
pellet	94	136	267	0.33	0.23	32.4
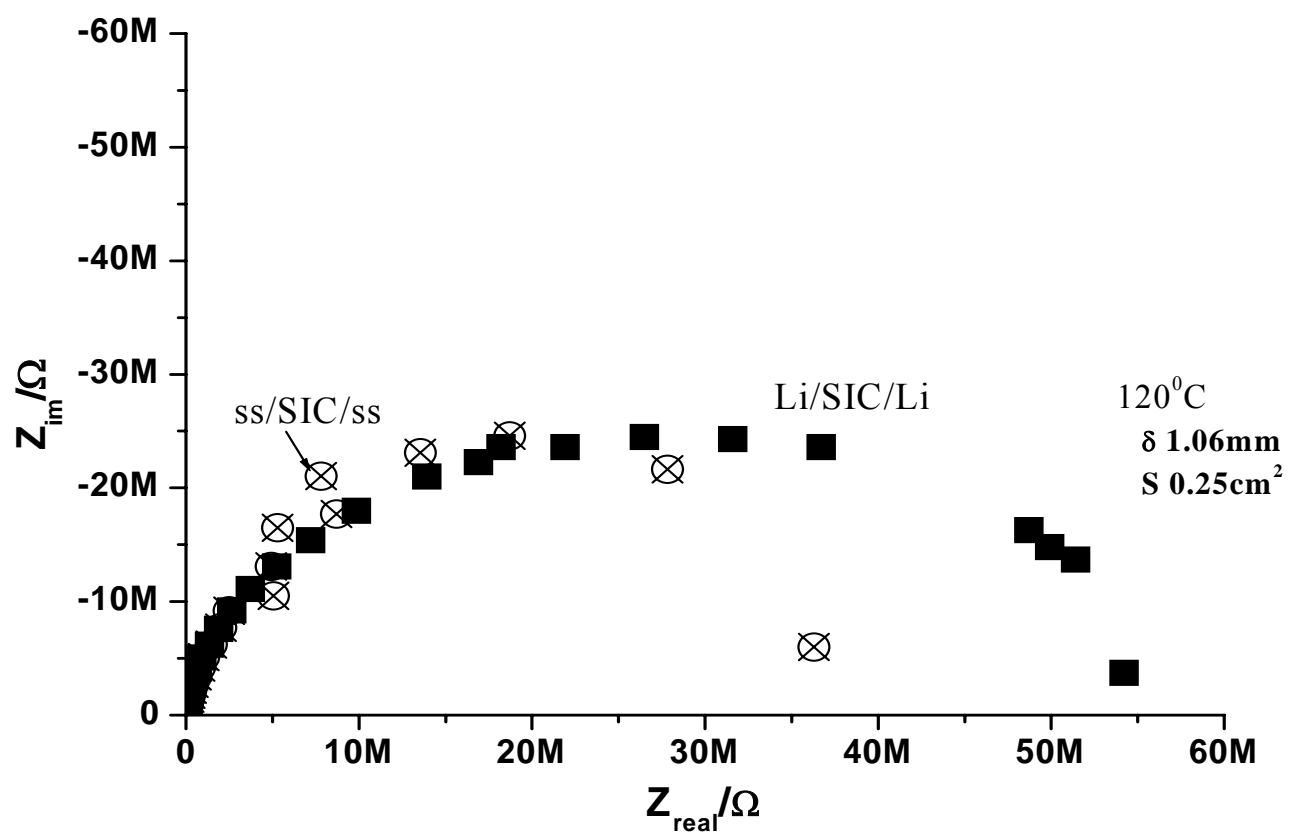
Fig.2.3. Nyquist plot of the cells composed of Li or s.s electrodes and $LiAlCl_4$:PAAM:EC pellet electrolyte
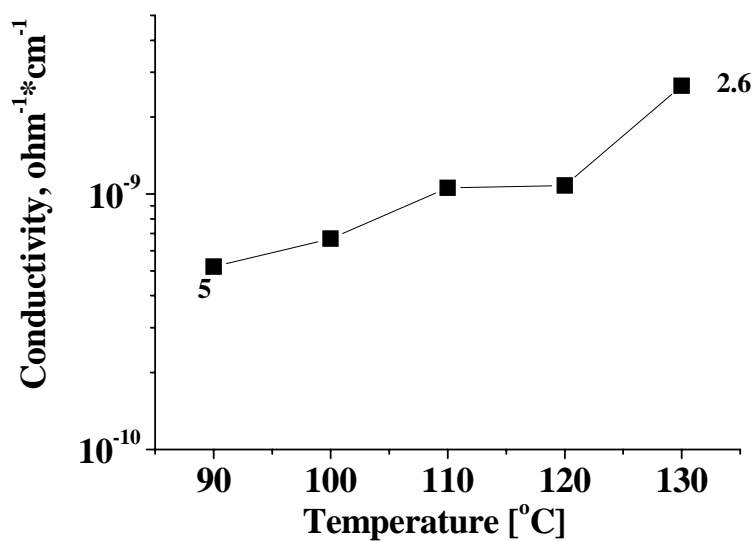
Fig. 2.4. Plot of ionic conductivity vs. temperature

The second polymer electrolyte sample from the University of Warsaw was received as a thin transparent film. Its composition is: co-polymer of 67.8 mol% of acrylonitrile with 32.2 mol% butyl acrylate and 72 w/w % (stoichiometrically with respect to AN) of $LiN(CF_3SO_2)_2$.

Fig.2.5 shows the SEM micrographs of the film. The SEM images differ at the edge and in the middle of the sample. It seems likely that at the edge, the polymer electrolyte has a rubber-like structure with incorporated islands of salt. In the middle, it has a homogeneous branch-like structure.

Two clear glass-transition points (at about -20°C and at 32.6°C are observed in the DSC trace (Fig. 2. 6). The polymer electrolyte is thermally stable up to 300°C.

AC impedance measurements of two types of cells - Au/SPE/Au and Li/SPE/Li - were performed. Nyquist plots of both SPE-cells with blocking and non-blocking electrodes are represented by a single depressed semicircle (Fig. 2.7). In order to calculate the ionic conductivity and SEI resistance, fitting of the experimental data was performed using a Z-PLOT program. The results of RC-fitting show that R_{bulk} is about twice that of R_{SEI} (Fig.28). The conductivity data extracted from the AC impedance plots of the cells with blocking and non-blocking electrodes are in good agreement. The ionic conductivity of the SPE at room temperature is about $1*10^{-9}$ S/cm and at 80 °C it is 3 to 4 orders of magnitude higher.
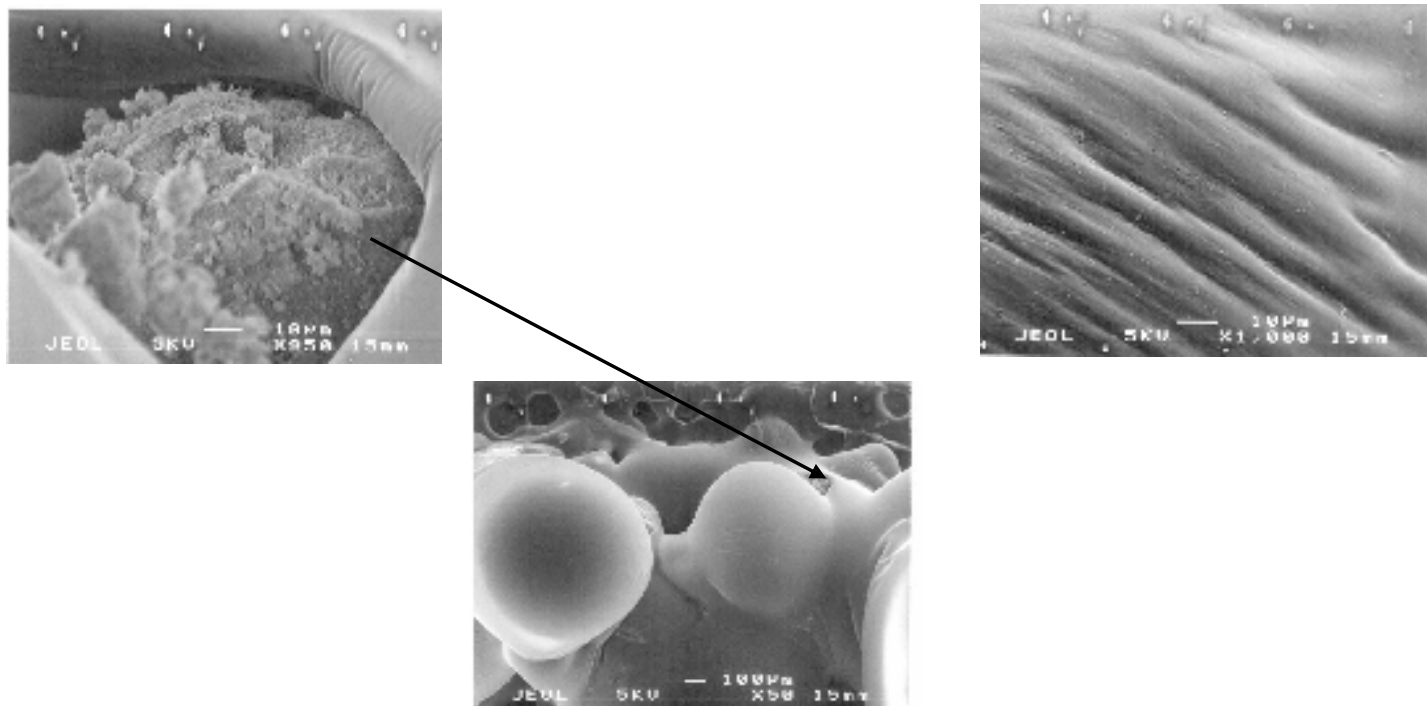
The edge of the film

The polymer electrolyte has a rubber-like structure with incorporated islands of salt
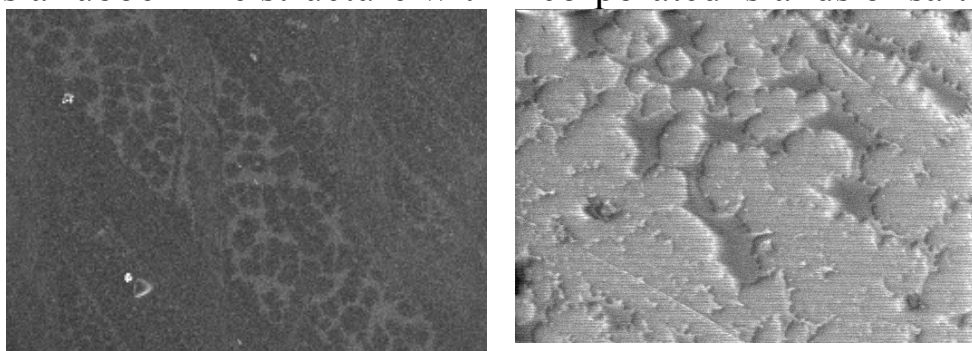
The middle of the film

Fig. 2.5. SEM images of the SPE film.

SPE based on the co-polymer of 67.8 mol% of acrylonitrile with 32.2 mol% butyl acrylate and 72 w/w % (stoichiometrically with respect to AN) of $LiN(CF_3SO_2)_2$.
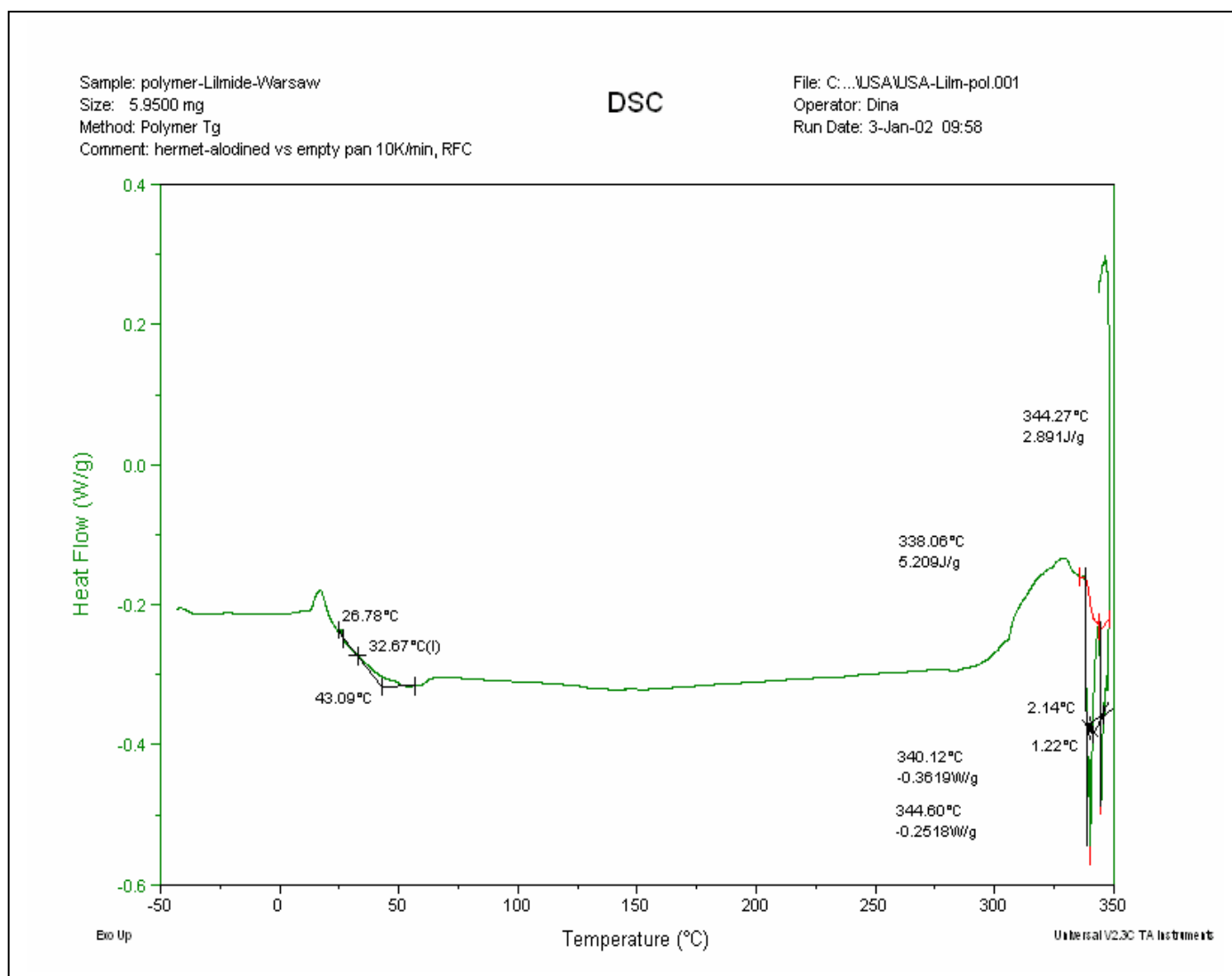
Fig. 2.6. The DSC thermogram of the SPE film.
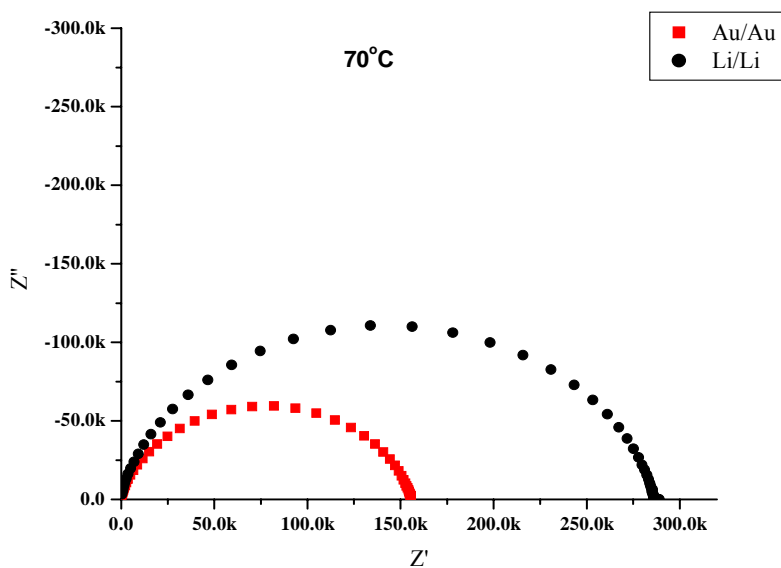
Fig.2.7. Nyquist plots of the Au/SPE/Au and Li/SPE/Li cells
SPE: co-polymer of 67.8 mol% of acrylonitrile with 32.2 mol% butyl acrylate and 72 w/w % (stoichiometrically with respect to AN) of $LiN(CF_3SO_2)_2$.
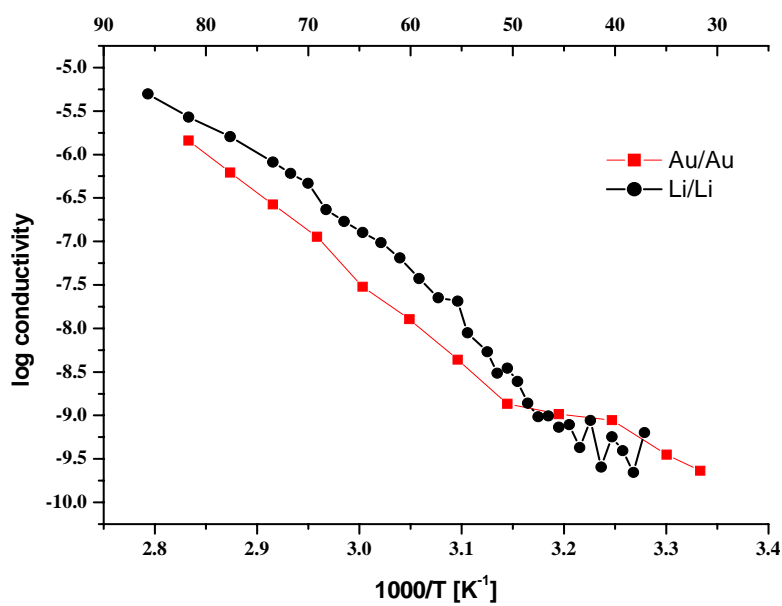
Fig.2.8. Arrhenius plots of the SPE
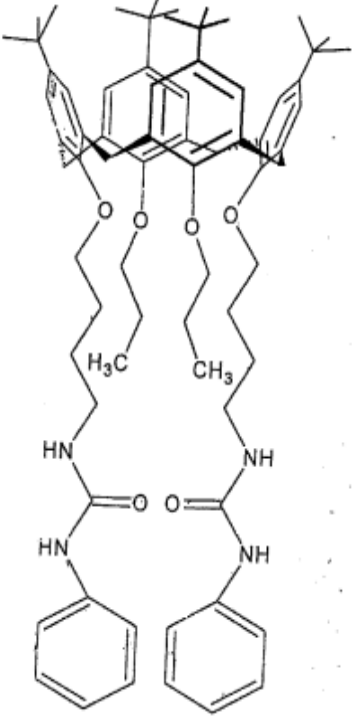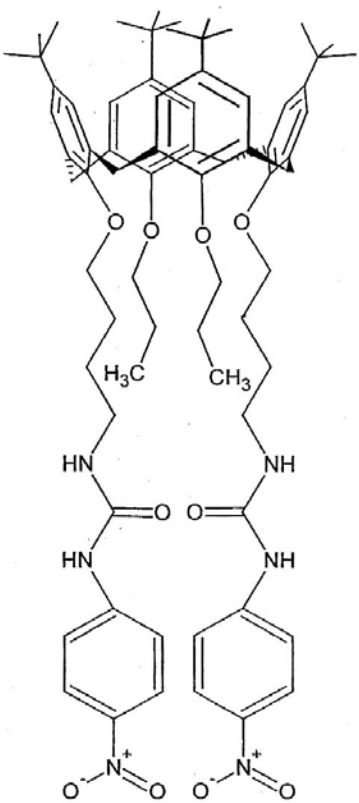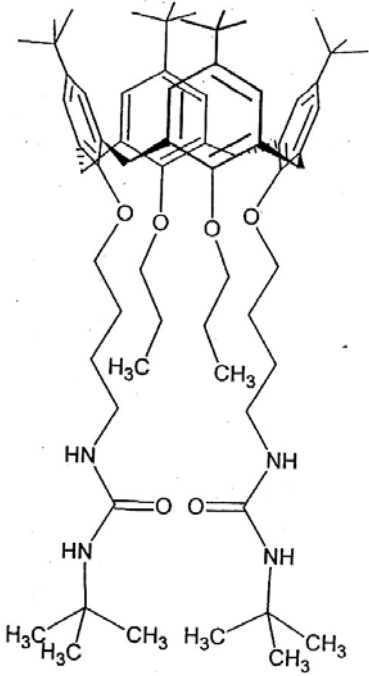
CHARACTERIZATION OF LiI-P(EO)$_n$ POLYMER ELECTROLYTES WITH CALIXARENE ADDITIVES.

In this work we attempted to increase t$_+$ by anion immobilization with calixarene, produced by a research group at the University of Warsaw. Three types of calixarene additive ($C_{72}H_{96}N_4O_6$ calixarene #1, $C_{72}H_{94}N_6O_{10}$ –calixarene #2, and $C_{68}H_{104}N_4O_6$ -calixarene #3) were tested.

LiI:P(EO)$_{20}$ and LiI:P(EO)$_7$ polymer electrolytes (PE) were prepared with three calixarene additives, structural formulas of which are shown in Table 2.1. It was almost impossible to obtain homogeneous LiI:P(EO)$_7$ films with high concentrations of additives, as increase of the calixarene concentration to 1M was followed by phase separation after evaporation of the acetonitrile.

Therefore, the LiI:calixarene molar ratio in the PEs studied did not exceed 1: 0.3.

Table 1. Structural formulas of calixarene additives

CALIXARENE#1- $C_{72}H_{96}N_4O_6$ MW= 1113.56 g/mole	CALIXARENE#2-$C_{72}H_{94}N_6O_{10}$ (TBPAN) MW =1203,55 g/mole	CALIXARENE#3-$C_{68}H_{104}N_4O_6$ (TBPAC) MW =1073,58 g/mole

Thermal analysis.

The thermal behavior of calixarene powders was tested by simultaneous TGA/DTA analysis.

As can be seen from the TGA tests (Fig. 2.9) the TBPAN (calixarene #2) sample is thermally stable up to 200 °C. The melting process, starting at 232 °C, is followed by decomposition of the TBPAN (calixarene #2) at 271.6 °C. The total weight loss of the sample is about 22%.

A small endotherm , which can be attributed to the melting of TBPAC (calixarene #3) appears in the DTA curve at 164 °C. Two-step decomposition of this compound starts at 214 °C with 3.3% weight loss. The second decomposition step occurs at 249 °C and is accompanied by a weight loss of 11%.
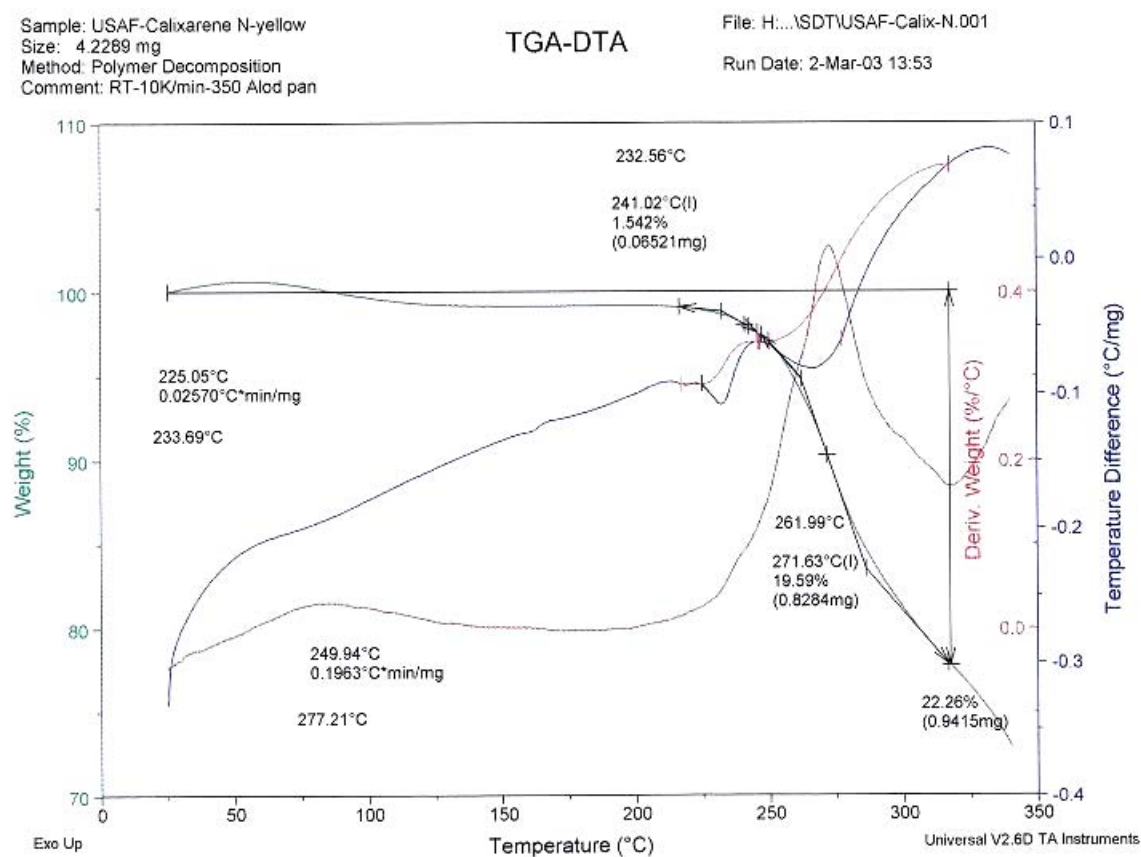
Fig. 2.9. Simultaneous TDA/DTA/DTG thermograms of the calixarene #2 powder
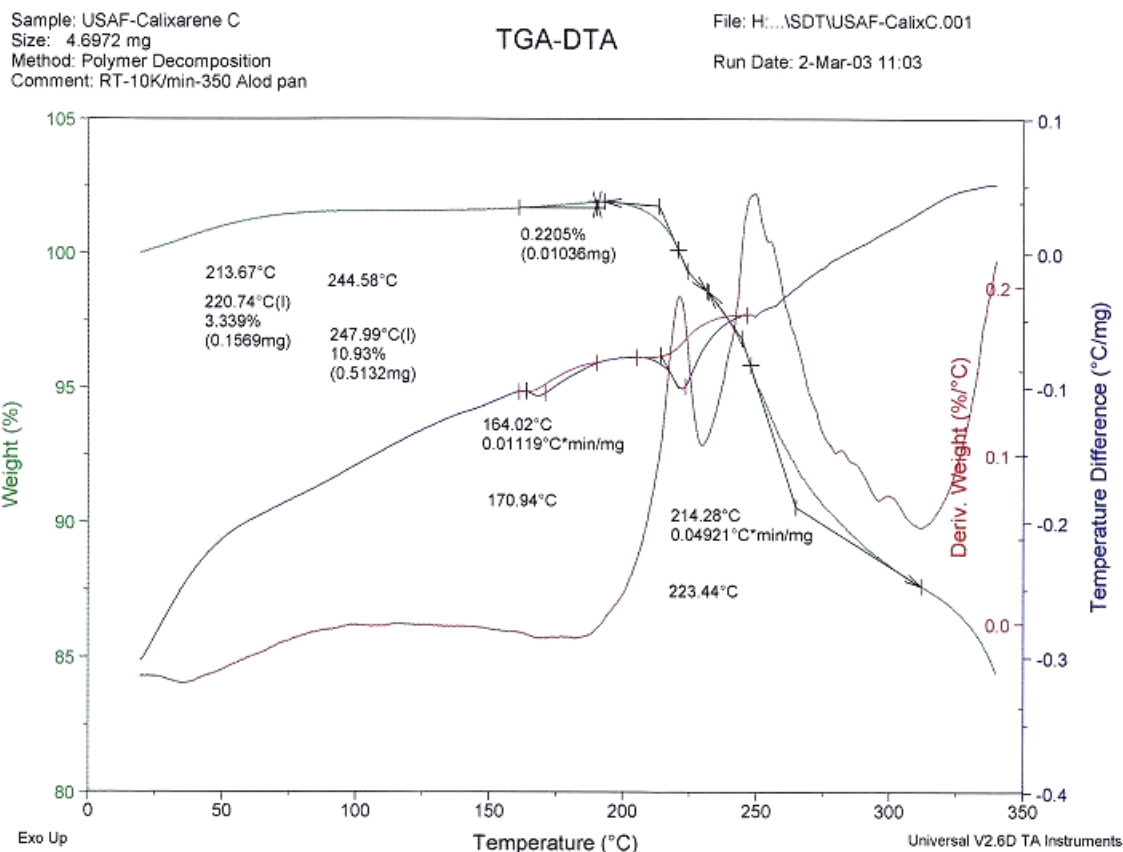
Fig.2.10. Simultaneous TDA/DTA/DTG thermograms of the calixarene #3 powder.

The DSC thermograms of the $LiI:P(EO)_{20}$ PEs with two different calixarene additives are shown in Figs.2.11a, b,c. All the DSC runs are characterized by a strong single endotherm at about 55°C. This peak is related to the melting of the LiI-P(EO) eutectic and excess of uncomplexed PEO. With increase of calixarene concentration the melting point falls, the enthalpy of the peak and its height decrease, thus indicating a decrease in the amount of the crystalline phase in the PE. The effect of calixarene #2 on the melting-point, enthalpy and peak height is stronger than that of calixarene #1. It should be emphasized that, contrary to the previously studied PEs with calixare #1 additive, the width of the melting peak decreases from 10.3 to 8.4 degrees with increase of the LiI- to-calixarene #2 ratio from 1:0.3 to 1:1. It was found that the melting peak of the PE with the highest concentration of calixarene #2 is the narrowest one (8.5 °C), thus indicating the highest order in the system. The sharp rise of the base line observed at above 250 °C in all the DSC traces of all the samples studied in this period is related to the decomposition of both the calixarene-iodide complex and the pure additive.

The DSC thermograms of the 1: 7 PEs with different calixarene additives are shown in Fig.2.11c. All the DSC runs are characterized by a pronounced high-temperature endotherm. A comparison of the

DSC data (Table 2) with those of the additive-free electrolyte, clearly shows that calixarene additives shift the melting transition toward higher temperatures by more than 100°C. The enthalpy of the DSC peak decreases sharply by a factor about of 2 to 5. In the additive-free PE, this peak was related to the melting of the LiI-P(EO) eutectic and excess of uncomplexed PEO. In the electrolyte containing additives, the high-temperature endotherm may be associated with the melting of a calixarene-salt-PEO complex. The exothermic transition at 250°C is related to the decomposition of calixarene compounds (see TGA curves in Figs 2.9. and Fig. 2.10). The absence of this exotherm in the DSC trace of PE with calixarene #2 may indicate the formation of a more stable additive-salt complex.
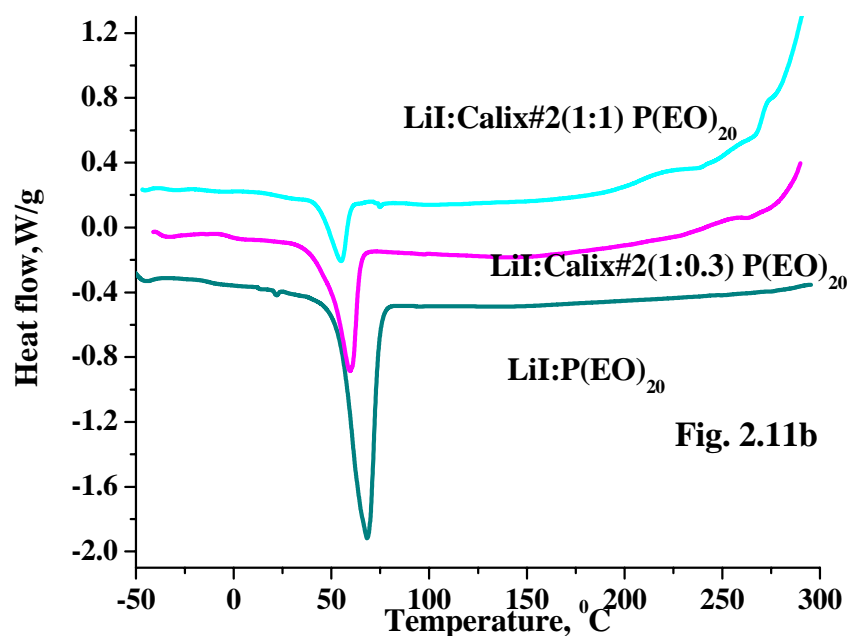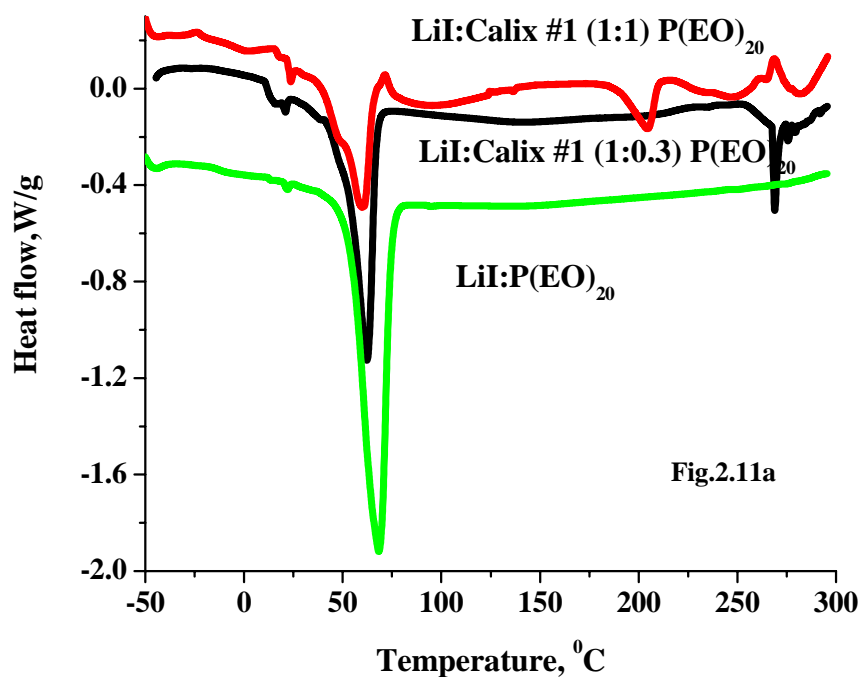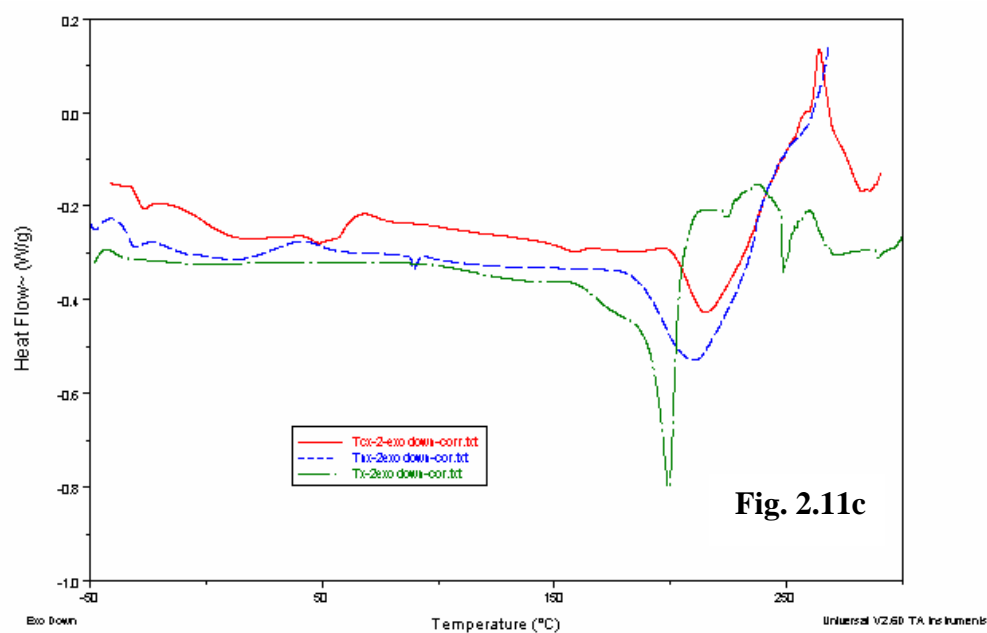
Fig.2.11a

Fig. 2.11b

Fig. 2.11. DSC thermograms of the LiI P(EO)$_{20}$ (7a, b) and Li P(EO)$_7$ (7c) polymer electrolyte with calixarene additives.

Table 2 represents the DSC data of all the PEs studied so far.

PE	ΔH, J/g	FWHM, ^{0}C	Height, W/g	T_{on}, ^{0}C
PEO	188	11.7	2.2	62
LiI:P(EO)$_7$	79.9	15.3	0.65	76
LiI:P(EO)$_7$ Calix#1 $_{0.3}$	45.4	9.9	0.55	189.8
LiI:P(EO)$_7$ Calix#2 $_{0.3}$	34.4	28.8	0.2	186.7
LiI:P(EO)$_7$ Calix#3 $_{0.3}$	17.8	20.4	0.15	202.6
LiI:P(EO)$_{20}$	122.9	12.5	1.46	53.7
LiI:P(EO)$_{20}$ Calix#1 $_{0.3}$	77.5	9.4	1.05	50.9
LiI:P(EO)$_{20}$ Calix#1 $_{1.0}$	50.1	14.6	0.55	47.2
LiI:P(EO)$_{20}$ Calix#2 $_{0.3}$	59.4	10.3	0.75	47.4
LiI:P(EO)$_{20}$ Calix#2 $_{1.0}$	22.0	8.5	0.36	43.6

Characterization of the morphology of LiI-P(EO)$_n$ PEs with calixarene additives.

From the SEM images of the PE samples (Fig.2.12) it is clear that the incorporation of low concentrations of calixarene #2 in the LiI:P(EO)$_{20}$ polymer electrolyte is followed by blurring of the grain boundaries. A PE with 1:1 salt to calixarene #2 ratio has needle-like surface morphology. In the SEM images of the LiI:P(EO)$_{20}$:(calix #3)$_{0.3}$ film, the individual grains cannot be distinguished either.
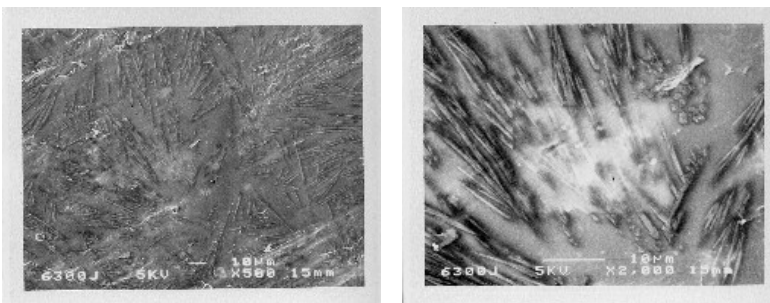
Without additive
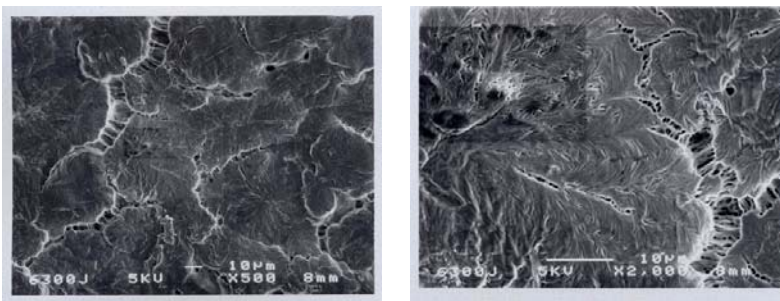
LiI:Calix#2=1:0.3
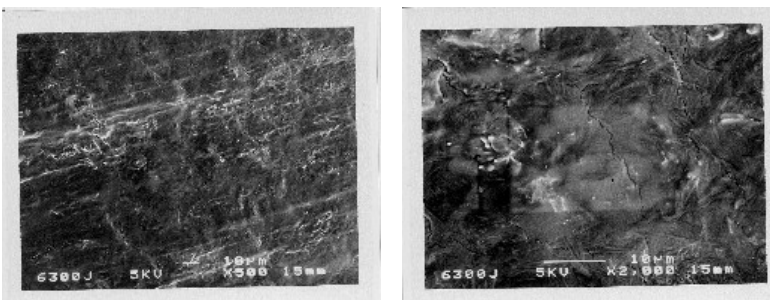
LiI:Calix#2=1:1

LiI:Calix#3=1:0.3
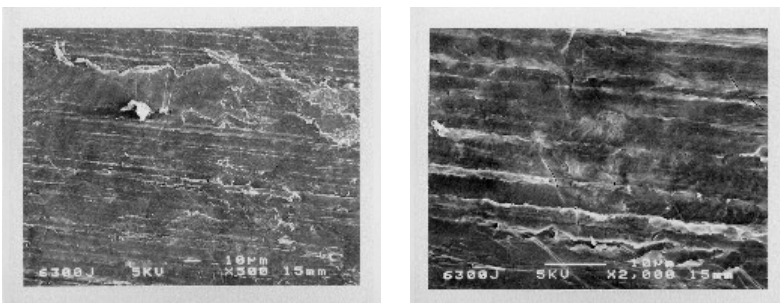
Fig. 2.12. SEM micrographs of the LiI:P(EO)$_{20}$ polymer electrolytes with calixarene additives

The morphology of LiI:P(EO)$_7$ polymer electrolytes (Fig. 2.13) strongly depends on the type of calixarene additive. The most homogeneous structure was found for calixarene #2.
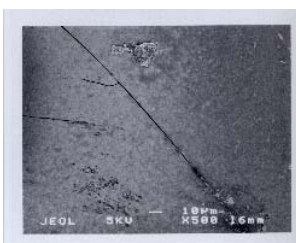
Without additive
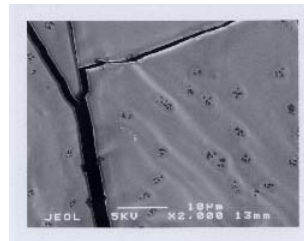
LiI:PEO$_7$:Calix#1 $_{0.3}$
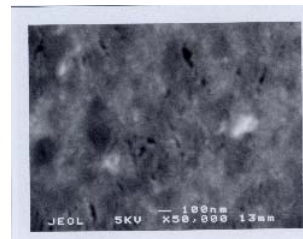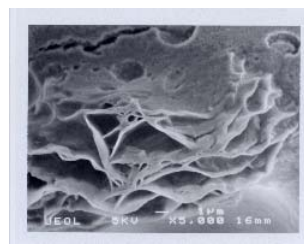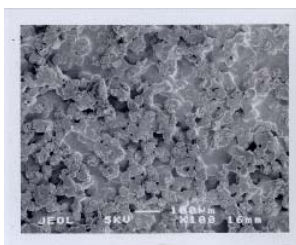

LiI:PEO$_7$:Calix#2 $_{0.3}$

LiI:PEO$_7$:Calix#3 $_{0.3}$

Fig. 2.13. SEM micrographs of the LiI:P(EO)$_7$ polymer electrolytes with calixarene additives

ELECTROCHEMICAL TESTS

Symmetrical lithium coin cells (type 2032) with different PEs were constructed and AC measurements were carried out. It was found that for all electrolytes studied with Li:EO ratios of both 20 and 7, the total resistance of the cells with calixarene additives is higher than that of the cells with pure PE samples. It seems likely that this is mainly caused by high GB resistance (inter-chain & inter-phase ion transport). Another possible explanation of this phenomenon is the reduced number of total charge carriers caused by the trapping of iodide anion by the calixarene additives.

Fig. 2.14 shows the bulk-conductivity (σ_{bulk}) data of the 1:20 PEs free of additives and containing different types and concentrations of calixarene. For electrolytes with low concentrations of calixarene, the bulk-conductivity values at ambient temperatures are close to those of the pure LiI P(EO)$_{20}$ electrolyte. Increase of temperature is followed by a considerable enhancement in the σ_{bulk} of pure electrolyte, while only a slight increase is detected in the σ_{bulk} of the PEs with 0.3M calixarene. It should be mentioned that, contrary to other additives, in the 1:20 PE with calixarene #3, the σ_{bulk} vs. T dependence is almost identical to that of the pure PE. The bulk conductivity of the 1:20 PEs with high concentration of calixarene #1 and #2 additives is half to a fifth that of the additive-free PE and PE with a LiI:calix ratio of 1:0.3 at RT. Above 60°C this difference increases to about two orders of magnitude and remains steady up to 110°C. This, in spite of the formation of a less crystalline structure that is quite the opposite of the behavior observed so far for PEO-based PEs. The negative effect of high concentrations of calixarene additives on the grain-boundary conductivity (σ_{GB}) is comparable with that on the σ_{Bulk} (see Fig. 2.15).
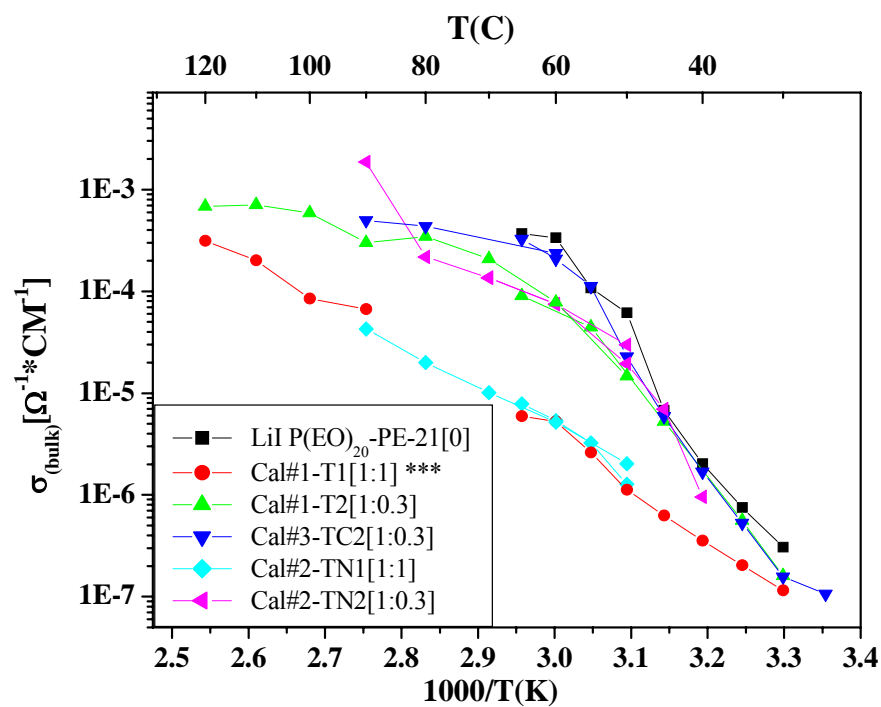
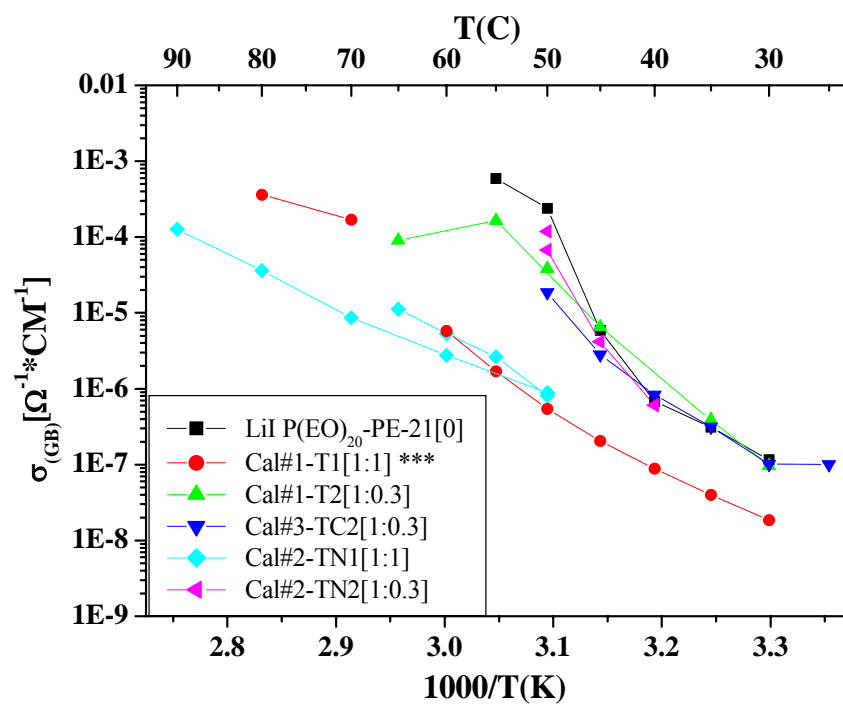Fig. 2.14. Bulk conductivity of the 1:20 polymer electrolytes under investigation

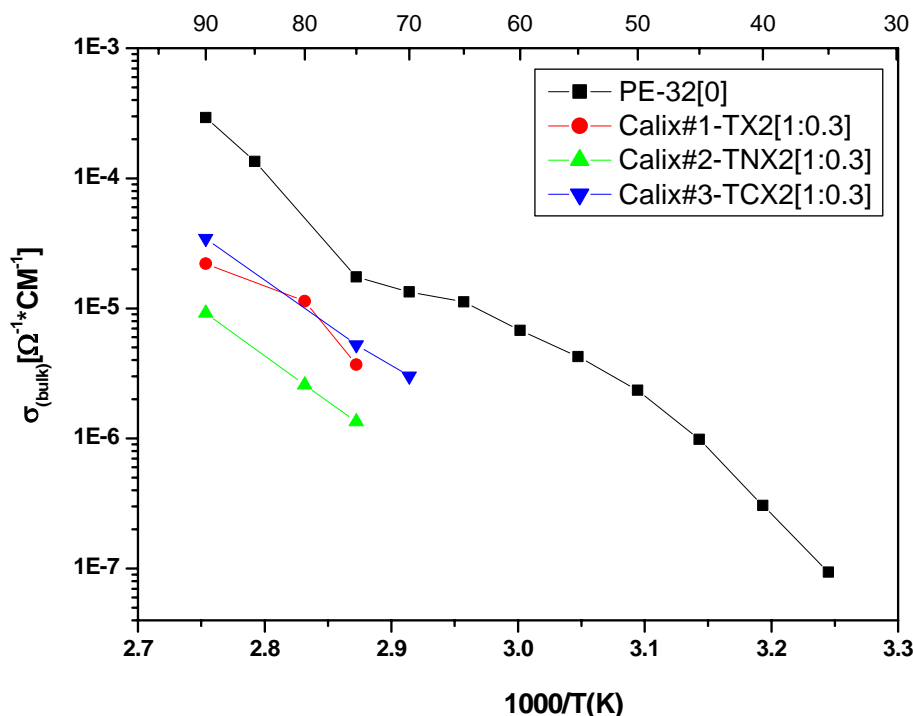Fig. 2.15. Grain-boundary conductivity of the 1:20 polymer electrolytes under investigation

Fig.2.16. Bulk conductivity of the 1:7 polymer electrolytes under investigation.

The Nyquist plot of LiI:P(EO)$_7$ PE is represented by a single depressed semicircle (not shown here). Below 70°C, because of the high impedance of the Li/PE+calixarene/Li cells, it was impossible calculate precisely the bulk, grain-boundary and SEI resistances. Above this temperature, the bulk conductivity of the additive-free electrolyte was 8 to 20 times that of the electrolyte containing calixarene(Fig. 2.16). A conductivity drop of two orders of magnitude was observed for an electrolyte with calixarene #2 additive. Similar results were obtained for the grain-boundary conductivity (Fig. 2.17). However, the lithium transference number in this PE (see Table 3 below) was the highest, indicating a strong anion-trapping effect of calixarene. The mechanism of ion conduction in such PEs is now under active study.
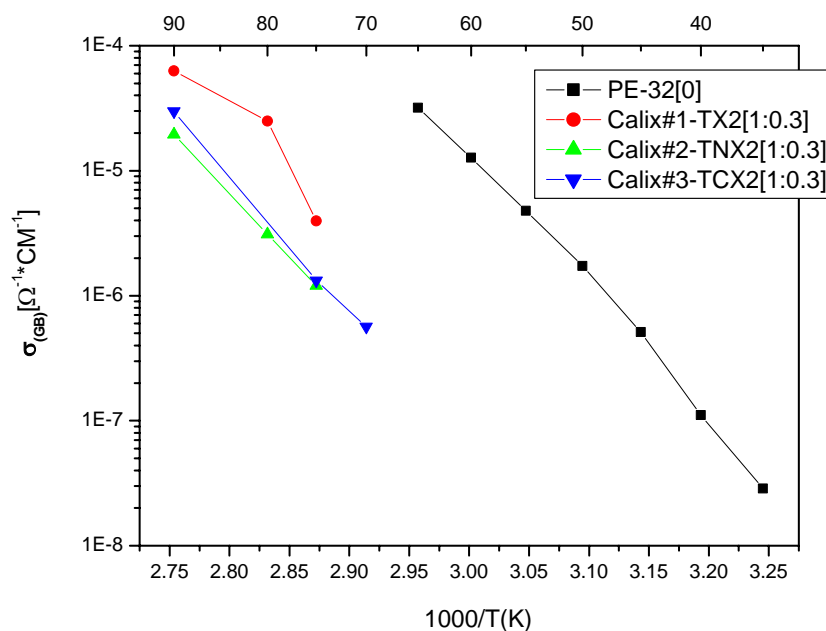
Fig.2.17. Grain-boundary conductivity of the 1:7 polymer electrolytes under investigation.

Fig. 2.18a shows the resistance of the SEI formed on the Li/PE interface. The resistance of the SEI decreases with increase in temperature in all the cells, but it is still much higher in the PE with high concentrations of calixarene #1 additive than that of the SEI formed on lithium in pure $LiI:P(EO)_{20}$. It is interesting that incorporation of calixarene #2 in the PE does not increase the interfacial resistance. R_{SEI} in cells with low concentrations of any calixarene additive is similar to that in additive-free PE. In the 1:7 electrolytes the most pronounced negative effect on the SEI was detected for calixarene #3 (Fig. 2.18b). Above 70°C, the R_{SEI} in the cells with low concentrations of any calixarene additive is close. The bulk, grain-boundary and SEI resistances were found to be almost unaffected by the time of storage of the PEs at 50 °C for more than 300 hours.
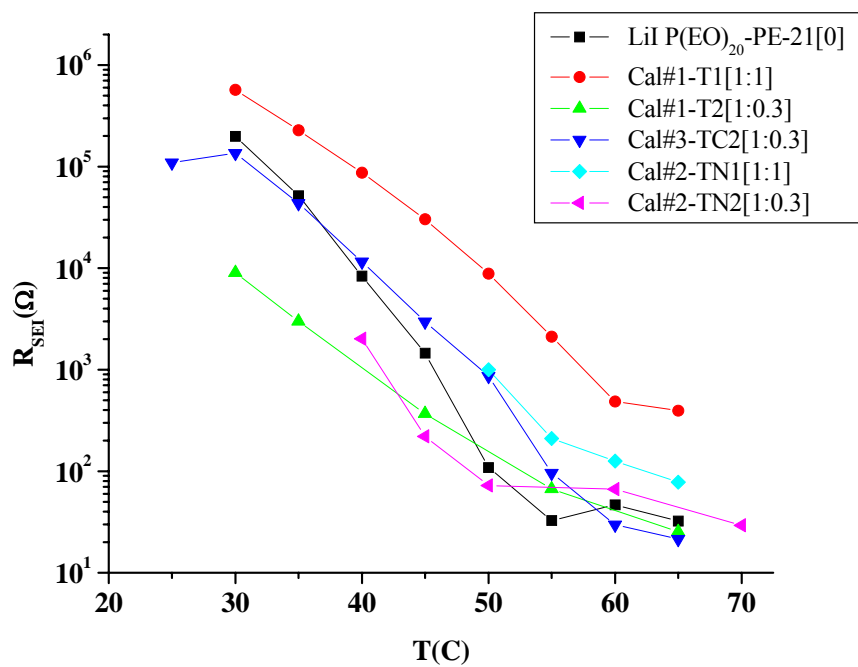
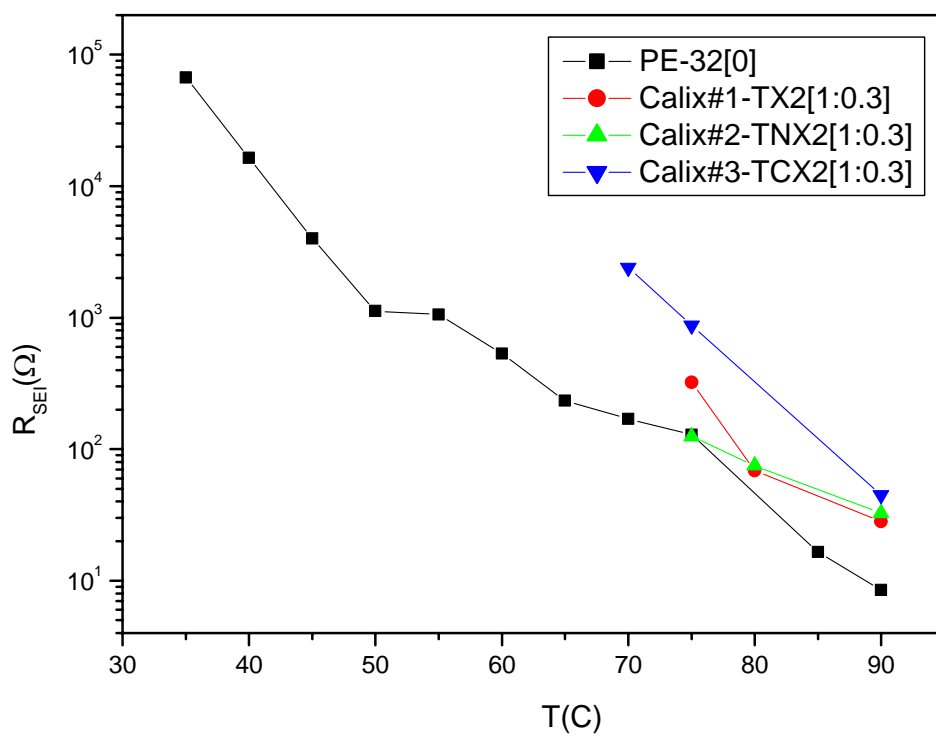Fig. 2.18a. R_{SEI} of the 1:20 polymer electrolytes under investigation.

Fig. 2.18b. R_{SEI} of the 1:7 polymer electrolytes under investigation.

Determination of lithium transference number.

The t_+ measurements were conducted according to the procedure developed by Bruce and improved by Scrosati. A constant voltage of 10mV was applied to the cell and the current-relaxation output was recorded as a function of time until steady state, which was typically reached after about one hour (Fig. 2.19). The current was stable for the remaining four hours of the measurement.
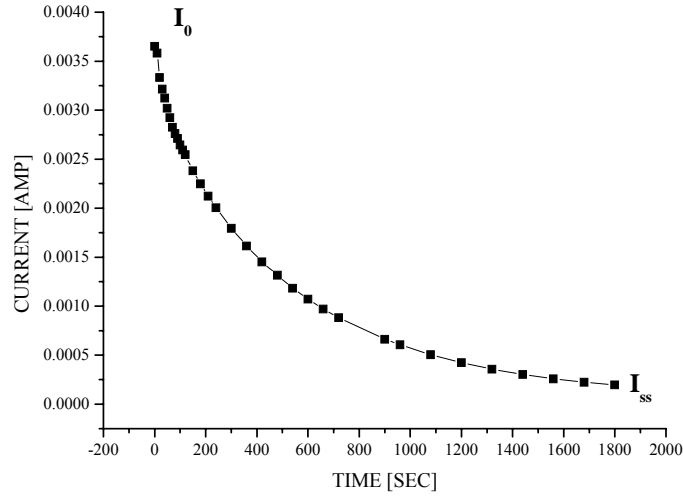
Fig, 2.19. Current-relaxation plot at 10 mV bias at 50°C.

t_+ was calculated according to the following equation (1).

$$t_+ = \frac{I_{SS}(\Delta V - I_0 R_0)}{I_0(\Delta V - I_{SS} R_{SS})}$$

R_0, R_{SS} - interfacial resistance R_{SEI} at initial and steady state.

Calculation of the diffusion coefficient of the cation (D_+) was carried out using the plot shown in Fig. 2.19 and equations (2) and (3):
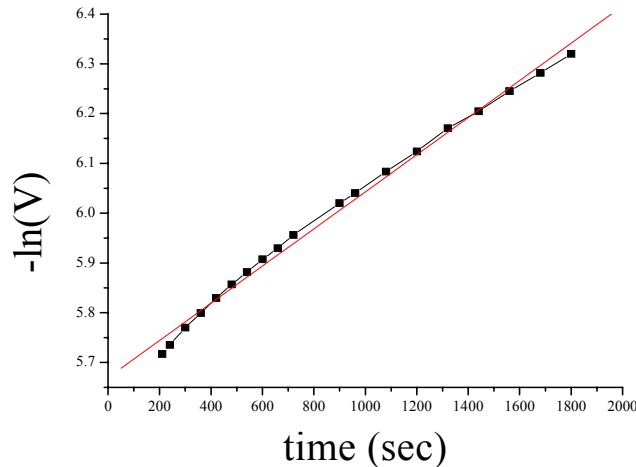
Fig. 2.20. Plot of ln (v) vs. time

$$D_S = \frac{A \times L^2}{\pi^2} \qquad (2)$$

where A- is the slope of the plot in Fig.2.20, L-thickness of polymer electrolyte

$$D_+ = \frac{D_S}{2(1+t_+)} \qquad (3)$$

The t_+ experimental data are presented in Tables 2.3 and 2.4.

Table 2.3. t_+ data for LiI:P(EO)$_{20}$ polymer electrolytes with Calixarene additives.

Polymer Type Li:EO=20	LiI:Calix ratio	Cell code	Exp.time, min	Voltage (V)	Temp (o C)	Transference number t_+	Diffusion coefficient D_+
PE-21	0	J-4	30	0.003	50	0.354	
PE-21	0	J-4	30	0.01	50	0.303	
PE-21	0	J-4	60	0.01	55	0.500	1.3E-8
T-1	#1 (1:1)	T16	30	0.003	50	0.364	
T-1	#1 (1:1)	T16	60	0.01	55	0.450	2.6E-9
T-2	#1 (1:0.3)	T15	30	0.003	50	0.585	
T-2	#1 (1:0.3)	T23	30	0.01	50	0.486	
T-2	#1 (1:0.3)	T23	30	0.01	55	0.450	
T-2	#1 (1:0.3)	T23	60	0.01	50	0.515	1.0E-9
T-2	#1 (1:0.3)	T15	60	0.01	55	0.480	1.0E-9
T-2	#1 (1:0.3)	T23	60	0.01	55	0.435	2.6E-9
TN-1	#2 (1:1)	T27/28	60	0.01	50	~1	
TN-1	#2 (1:1)	T27/28	60	0.01	60	~1	
TN-1	#2 (1:1)	T27/28	60	0.01	70	~1	
TN-1	#2 (1:1)	T27	60	0.01	80	0.762	
TN-1	#2 (1:1)	T28	60	0.01	80	0.700	2.6E-9
TN-2	#2 (1:0.3)	T15	30	0.01	50	0.474	
TN-2	#2 (1:0.3)	T23	60	0.1	50	0.513	1.0E-9
TC-2	#3 (1:0.3)	T-29	60	0.01	70(down from 90)	0.644	1.2e-8

As can be seen from Table 2.3, the LiI (PEO)$_{20}$ polymer electrolyte with 1:1 LiI-to-calixarene #2 has t_+ =1 at 50 to 70 °C. At 80 °C the lithium transference number decreases to about 0.70-0.76. These data are supported by the Nyquist plots of the symmetric Li/PE cell, recorded at 60 °C, where the diffusion branch does not appear even at the very low frequency of 2mHz (Fig.2.21). In the Nyquist plot of the same cell at 80 °C (Fig. 2.22) the diffusion tail can be observed at 10mHz, indicating lowering of the t_+.
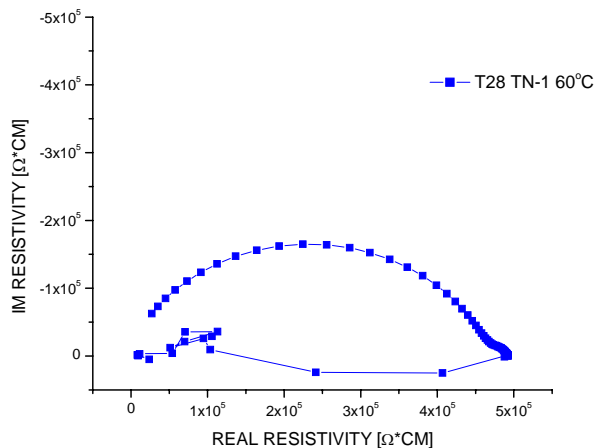

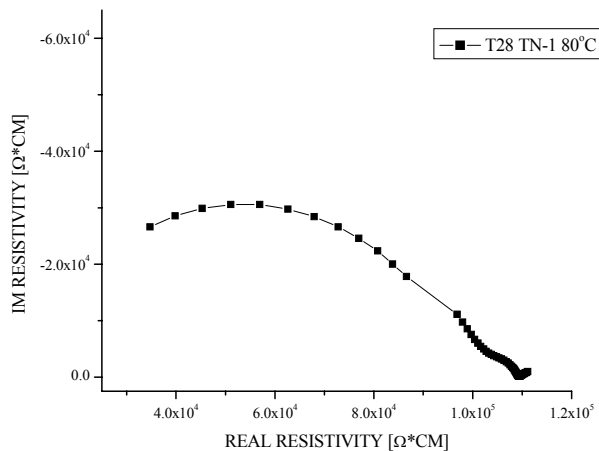Fig.2.21. Nyquist plot of the Li/ LiI$_1$ (PEO)$_{20}$ (calixarene #3)1/Li cell, recorded at 60 °C

Fig.2.22. Nyquist plot of the Li/ LiI$_1$ (PEO)$_{20}$ (Calixarene#3)$_1$/Li cell, recorded at 80 °C

As can be seen from Table 2.4, the pure LiI(PEO)$_7$ polymer electrolyte has the t_+ about 0.51 at 50 to 90 °C. The incorporation of Calixarene#1 additive is followed by the t_+ drop to 0.2-0.3. Calixarene #2 and #3 additives increase t_+ up to 0.7. At 90 °C, the lithium transference number in PE containing 0.3M calixarene#3 sharply decreases to about 0.3. The similar negative temperature effect on the

transference number was observed in the LiI(PEO)$_{20}$ PEs. However, the diffusion coefficient of lithium ion increases with temperature. The observed phenomena may indicate that the calixarene-induced ordering of the PEs and trapping of the anion, highly pronounced at near ambient temperatures, is less effective on heating.

Table 2.4. t$_+$ data for LiI:P(EO)$_7$ polymer with Calixarene additives.

PE composition	Polymer Code	Cell #	Temp (^{o}C)	Transference number t$_+$	Diffusion coefficient D$_+$
LiI:P(EO)$_7$	PE-32	J-8	55	0.508	3.00e-9
LiI:P(EO)$_7$	PE-32	J-8	75	0.556	1.44e-8
LiI:P(EO)$_7$	PE-32	J-8	90	0.513	4.65e-8
LiI:P(EO)$_7$:Cal#1 $_{0.3}$	TX-2	X-2	75	0.35	4.51e-9
LiI:P(EO)$_7$:Cal#1 $_{0.3}$	TX-2	X-2	90	0.24	6.95e-9
LiI:P(EO)$_7$:Cal#2 $_{0.3}$	TNX-2	X-4	75	0.743	2.10e-9
LiI:P(EO)$_7$:Cal#2 $_{0.3}$	TNX-2	X-3	90	0.690	7.42e-9
LiI:P(EO)$_7$:Cal#3 $_{0.3}$	TCX-2	X-5	75	0.700	-
LiI:P(EO)$_7$:Cal#3 $_{0.3}$	TCX-2	X-5	90	0.330	2.78e-8

However, the Calixarene additives were found to be inactive as traps for another lithium salt anions. With the aim to overcome this problem Warsaw group synthesized a new 1,1,3,3,5,5-mezo-hexaphenyl-2,2,4,4,6,6-mezo-hexamethyl-6-pyrrole compound, which, in addition to LiI, was expected to complex other anions as well.

This brief report presents the characterization of concentrated LiX-P(EO)$_{20}$ and LiX-P(EO)$_7$ polymer electrolytes with Calixpyrrole additive (C$_6$P-abbreviation). Three lithium salts (LiI, LiTF and LiClO$_4$) are under investigation. At least 2-3 Li/PE/Li cells were assembled and tested to check the reproducibility of experimental data.

On the basis of the results of our previous work, in which a lithium transference number of unity was achieved in PEs with salt-to-additive ratio 1:1, a series of polymer electrolytes with the same concentration ratios was prepared. As can be seen from Table 2.5, in contrast to our previous results, addition of C$_6$P to the LiI:P(EO)$_{20}$ polymer electrolyte is followed by a significant decrease of t$_+$. For

the lithium triflate electrolyte, however, high t_+ varying from 0.6 to 0.78 were measured a wide temperature range.

Table 2.5. Lithium transference number (Lithium salt-to-additive ratio=1)

PE composition	Cell code	Temp, °C	t_+
LiI:PEO$_{20}$	J-4	55	0.5
LiI:PEO$_{20}$:C$_6$P	CI-1	50	0.18
LiI:PEO$_{20}$:C$_6$P	NI-4	50	0.14
LiTf:PEO$_{20}$	J12	60	0.26
-"-	J12	75	0.45
-"-	J12	90	0.73
LiTf:PEO$_{20}$:C$_6$P	NT-1	55	0.74
-"-	NT-1	60	0.65
-"-	NT-1	75	0.58
-"-	NT-1	90	0.64
-"-	NT-1	120	0.75
LiTf:PEO$_{20}$:C$_6$P	CT-4	55	0.63
-"-	CT-4	60	0.53
-"-	CT-4	75	0.63
-"-	CT-4	90	0.6
-"-	CT-4	120	0.7

a
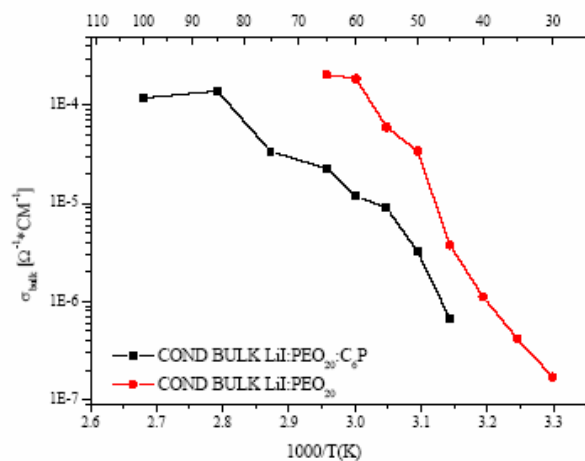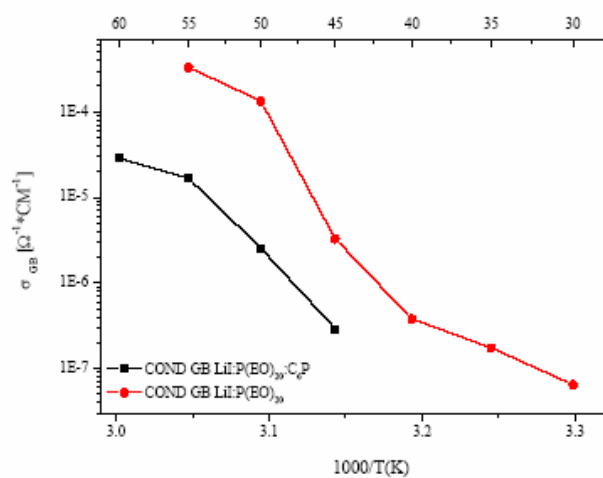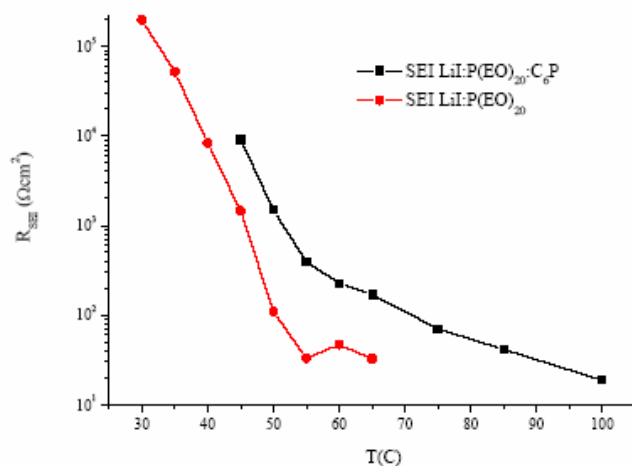

b

c

Fig. 2.23. Temperature dependence of the bulk (a), grain boundary (b) conductivity and interphase resistance (c) of the LiI:P(EO)$_{20}$ polymer electrolytes with and without additive. Red curves - LiI:P(EO)PE without additives , black curves LiI: P(EO): CP.

Addition of calixpyrrole (C$_6$P) to the LiI::P(EO)$_{20}$ PE is followed by a 5- to 9 time decrease magnitude in both bulk and grain boundary conductivity (Figs.2.23a, b). The solid-electrolyte-interphase resistance of the electrolyte containing C$_6$P is about 6 times larger. It should be noted that the negative effect of the calixpyrrole additive on the conductivity drop is less pronounced than in concentrated LiI-based electrolytes with calixarene additive studied previously.

The opposite effect of calixpyrrole additive on the bulk and grain boundary conductivity was detected in LiTf:P(EO)$_{20}$ PE. The bulk conductivity of the C$_6$P-containing electrolyte at near ambient temperatures was almost one order of magnitude higher than the σ_{bulk} of additive-free PE, and two orders of magnitude higher than that of electrolytes containing calixarene #2 (Fig. 2.24a). Above 70°C, σ_{bulk} values of the first two PEs are similar. A semicircle attributed to grain-boundary conductivity was detected in the Nyquist plot of Li/ LiTf:P(EO)$_{20}$:C$_6$P /Li cell up to 60°C only (not shown here), indicating low GB resistance in this electrolyte (Fig. 2.24b). In addition, the resistance of the SEI was significantly lower in LiTf:P(EO)$_{20}$:C$_6$P PE (Fig. 2.24c). Such a positive effect of calixpyrrole additive on the electrochemical properties of the lithium triflate-based polymer electrolyte deserves attention and further investigation.

LiI:P(EO)₇, LiTF:P(EO) and LiClO₄:P(EO)₇ PEs

After evaporation of the acetonitrile and room-temperature vacuum drying for 48 hours all the films were extremely viscous and it was practically impossible to separate them from the Teflon tray. In addition strong phase separation was observed.

Additional attempt will be undertaken to prepare these concentrated electrolytes using acetonitrile- dichloromethne mixture of solvents aaccording to a procedure developed by Prof. Scrosati group. Structural and thermal characteristics of the PEs with calixpyrrole additive are being tested.
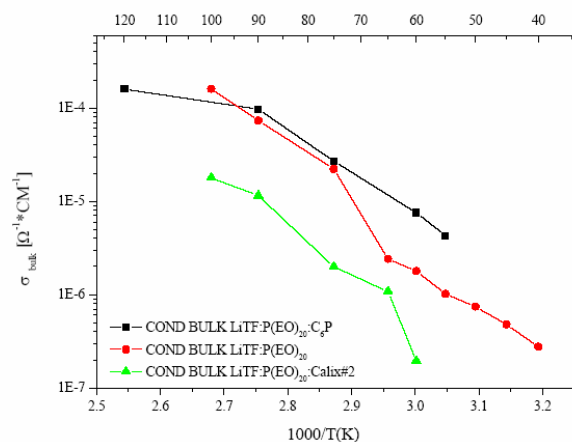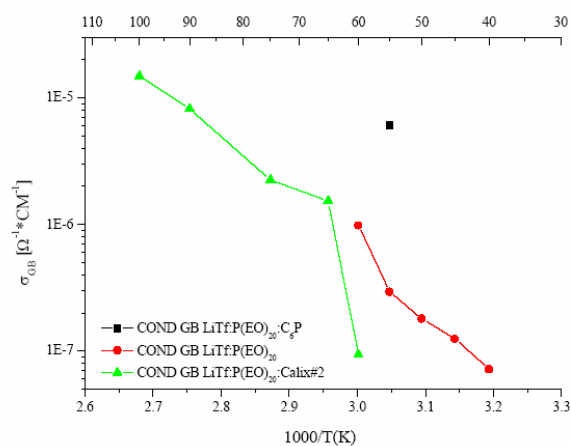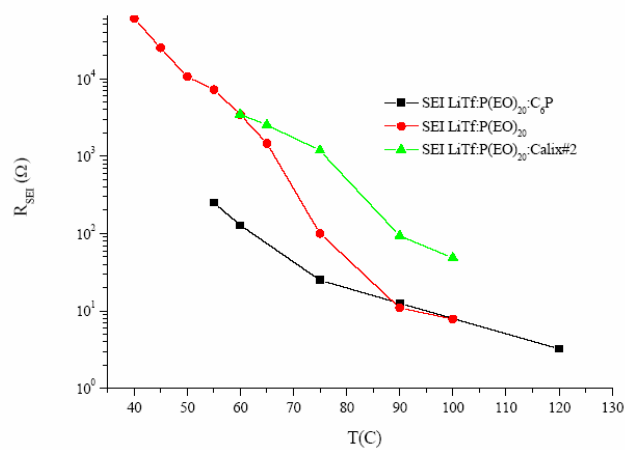
a

b

c

Fig. 2.24 Temperature dependence of the bulk (a), grain boundary (b) conductivity and interphase resistance of the LiTf:P(EO)$_{20}$: (red curves), LiTf:P(EO)$_{20}$:C$_6$P and LiTf:P(EO)$_{20}$:TBPAN1 (green curves) polymer electrolytes.

Conclusions

1.   Development and characterization of thin-film iron sulfide cathodes by RF-sputtering and electrodeposition was carried out. X-ray diffraction (XRD), SEM and X-ray photoelectron spectroscopy (XPS) tests indicated that submicron to several micron-thick electrodeposited FeS_x films have an amorphous, network-like porous structure with nano-size particles. The deposit is a mixture of iron mono- and disulfide, and non-stoichiometric FeS_{1+x} phases with some iron oxides. RF-sputtered cathodes are highly crystalline. Our experimental findings show considerable promise of creating sulfur-deficient pyrite structure for cathodes to be used in high-energy-density all-solid-state lithium batteries.

2.   Li/CPE/FeS_x cells ran at $i_d = i_{ch} = 50$ $\mu A/cm^2$ and 125°C for over 650 charge/discharge cycles with 0.01 to 0.06%/cycle capacity loss and 100% Faradaic efficiency. On the basis of the experimental data it can be deduced that this simple electrodeposition method shows great promise for the preparation of ultra-thin cathodes for rapid characterization of other components. These electrodes can be used for microbattery applications.

3.   New types of solid polymer electrolytes formed by adding a suitable anion-trapping calixarene and calixpyrrole additives to a PEO-LiX complex have been developed and characterized. The results demonstrate that these electrolytes have unique properties, i.e. a lithium ion transport number equal to one combined with an appreciable conductivity.